

Magnetization Dynamics in Synthetic Antiferromagnets with Perpendicular Magnetic Anisotropy

Dingbin Huang^{1,*}, Delin Zhang², Yun Kim¹, Jian-Ping Wang², and Xiaojia Wang^{1,*}

¹Department of Mechanical Engineering, University of Minnesota, Minneapolis, MN 55455, USA

²Department of Electrical and Computer Engineering, University of Minnesota, Minneapolis, MN 55455, USA

ABSTRACT:

Understanding the rich physics of magnetization dynamics in perpendicular synthetic antiferromagnets (p-SAFs) is crucial for developing next-generation spintronic devices. In this work, we systematically investigate the magnetization dynamics in p-SAFs combining time-resolved magneto-optical Kerr effect (TR-MOKE) measurements with theoretical modeling. These model analyses, based on a Landau-Lifshitz-Gilbert approach incorporating exchange coupling, provide details about the magnetization dynamic characteristics including the amplitudes, directions, and phases of the precession of p-SAFs under varying magnetic fields. These model-predicted characteristics are in excellent quantitative agreement with TR-MOKE measurements on an asymmetric p-SAF. We further reveal the damping mechanisms of two precession modes co-existing in the p-SAF and successfully identify individual contributions from different sources, including Gilbert damping of each ferromagnetic layer, spin pumping, and inhomogeneous broadening. Such a comprehensive understanding of magnetization dynamics in p-SAFs, obtained

*Authors to whom correspondence should be addressed: huan1746@umn.edu and wang4940@umn.edu

by integrating high-fidelity TR-MOKE measurements and theoretical modeling, can guide the design of p-SAF-based architectures for spintronic applications.

KEYWORDS: Synthetic antiferromagnets; Perpendicular magnetic anisotropy; Magnetization Dynamics; Time-resolved magneto-optical Kerr effect; Spintronics

1 INTRODUCTION

Synthetic antiferromagnetic (SAF) structures have attracted considerable interest for applications in spin memory and logic devices because of their unique magnetic configurations [1-3]. The SAF structures are composed of two ferromagnetic (FM) layers anti-parallelly coupled through a non-magnetic (NM) spacer, offering great flexibilities for the manipulation of magnetic configurations through external stimuli (*e.g.*, electric-field and spin-orbit torque, SOT). This permits the design of new architectures for spintronic applications, such as magnetic tunnel junction (MTJ), SOT devices, domain wall devices, skyrmion devices, among others [4-7]. The SAF structures possess many advantages for such applications, including fast switching speeds (potentially in the THz regimes), low offset fields, small switching currents (and thus low energy consumption), high thermal stability, excellent resilience to perturbations from external magnetic fields, and large turnability of magnetic properties [3,8-16].

A comprehensive study of the magnetization dynamics of SAF structures can facilitate the understanding of the switching behavior of spintronic devices, and ultimately guide the design of novel device architectures. Different from a single FM free layer, magnetization dynamics of the SAF structures involves two modes of precession, namely high-frequency (HF) and low-frequency (LF) modes, that result from the hybridization of magnetizations precession in the two FM layers. The relative phase and precession amplitude in two FM layers can significantly affect the spin-pumping enhancement of magnetic damping [17], and thus play an important role in determining the magnetization dynamic behaviors in SAFs. Heretofore, the exchange-coupling strength and magnetic damping constant of SAFs have been studied by ferromagnetic resonance (FMR) [18-21] and optical metrology [22-25]. Most FMR-based experimental studies were limited to SAFs with in-plane magnetic anisotropy (IMA). For device applications, perpendicular magnetic

anisotropy (PMA) gives better scalability [3,26]. Therefore, the characteristics of magnetization dynamics of perpendicular SAF (p-SAF) structures are of much value to investigate. In addition, prior studies mainly focused on the mutual spin pumping between two FM layers [22,27,28]. A more thorough understanding of the contributions from various sources, including inhomogeneous broadening [29], remains elusive.

In this paper, we report a comprehensive study of the magnetization dynamics of p-SAFs by integrating high-fidelity experiments and theoretical modeling to detail the characteristic parameters. These parameters describe the amplitude, phase, and direction of magnetization precession of both the HF and LF modes for the two exchange-coupled FM layers in a p-SAF. We conduct all-optical time-resolved magneto-optical Kerr effect (TR-MOKE) measurements [30-33] on an asymmetric p-SAF structure with two different FM layers. The field-dependent amplitude and phase of TR-MOKE signals can be well captured by our theoretical model, which in turn provides comprehensive physical insights into the magnetization dynamics of p-SAF structures. Most importantly, we show that inhomogeneous broadening plays a critical role in determining the effective damping of both HF and LF modes, especially at low fields. We demonstrate the quantification of contributions from inhomogeneous broadening and mutual spin pumping (*i.e.*, the exchange of angular momentum between two FM layers via pumped spin currents) [21] to the effective damping, enabling accurate determination of the Gilbert damping for individual FM layers. Results of this work are beneficial for designing p-SAF-based architectures in spintronic applications. Additionally, this work also serves as a successful example demonstrating that TR-MOKE, as an all-optical metrology, is a powerful tool to capture the magnetization dynamics and reveal the rich physics of complex structures that involve multilayer coupling.

2 METHODOLOGY

2.1 Sample preparation and characterization

One SAF structure was deposited onto thermally oxidized silicon wafers with a 300-nm SiO₂ layer by magnetron sputtering at room temperature (RT) in a six-target ultra-high vacuum (UHV) Shamrock sputtering system. The base pressure is below 5×10^{-8} Torr. The stacking structure of the SAF is: [Si/SiO₂]_{sub}/[Ta(5)/Pd(3)]_{seed}/[Co(0.4)/Pd(0.7)/Co(0.4)]_{FM1}/[Ru(0.6)/Ta(0.3)]_{NM}/CoFeB(1)_{FM2}/[MgO(2)/Ta(3)]_{capping}. The numbers in parentheses denote the layer thicknesses in nanometers. After deposition, the sample was annealed at 250 °C for 20 minutes by a rapid-thermal-annealing process. The two FM layers are CoFeB and Co/Pd/Co layers, separated by a Ru/Ta spacer, forming an asymmetric p-SAF structure (*i.e.*, two FM layers having different magnetic properties). The M - H_{ext} loops were characterized by a physical property measurement system (PPMS) with a vibrating-sample magnetometer (VSM) module. The resulting M - H_{ext} loops are displayed in Fig. 1(a). Under low out-of-plane fields ($H_{\text{ext}} < 500$ Oe), the total magnetic moments in two FM layers of the SAF stack perfectly cancel out each other: $M_1 d_1 = M_2 d_2$ with M_i and d_i being the magnetization and thickness of each FM layer ($i = 1$ for the top CoFeB layer and $i = 2$ for the bottom Co/Pd/Co layer). The spin-flipping field ($H_f \approx 500$ Oe) in the out-of-plane loop indicates the bilinear interlayer-exchange-coupling (IEC) J_1 between the two FM layers: $J_1 = -H_f M_{s,1} d_1 \approx -0.062$ erg cm⁻² [34]. The values of $M_{s,1}$, $M_{s,2}$, d_1 , and d_2 can be found in Table SI of the Supplemental Material (SM) [35].

2.2 Theoretical foundation of magnetization dynamics for a p-SAF structure

The magnetic free energy per unit area for a p-SAF structure with uniaxial PMA can be expressed as [36]:

$$\begin{aligned}
F = & -J_1(\mathbf{m}_1 \cdot \mathbf{m}_2) - J_2(\mathbf{m}_1 \cdot \mathbf{m}_2)^2 \\
& + \sum_{i=1}^2 d_i M_{s,i} \left[-\frac{1}{2} H_{k,\text{eff},i} (\mathbf{n} \cdot \mathbf{m}_i)^2 - \mathbf{m}_i \cdot \mathbf{H}_{\text{ext}} \right]
\end{aligned} \tag{1}$$

where J_1 and J_2 are the strength of the bilinear and biquadratic IEC. $\mathbf{m}_i = \mathbf{M}_i / M_{s,i}$ are the normalized magnetization vectors for individual FM layers ($i = 1, 2$). d_i , $M_{s,i}$, and $H_{k,\text{eff},i}$ denote, respectively, the thickness, saturation magnetization, and the effective anisotropy field of the i -th layer. \mathbf{n} is a unit vector indicating the surface normal direction of the film. For the convenience of derivation and discussion, the direction of \mathbf{m}_i is represented in the spherical coordinates by the polar angle θ_i and the azimuthal angle φ_i , as shown in Fig. 1(b).

The equilibrium direction of magnetization in each layer $(\theta_{0,i}, \varphi_{0,i})$ under a given \mathbf{H}_{ext} is obtained by minimizing F in the $(\theta_1, \varphi_1, \theta_2, \varphi_2)$ space. The magnetization precession is governed by the Landau-Lifshitz-Gilbert (LLG) equation considering the mutual spin pumping between two FM layers [27,37-40]:

$$\frac{d\mathbf{M}_i}{dt} = -\gamma_i \mathbf{M}_i \times \mathbf{H}_{\text{eff},i} + \frac{(\alpha_{0,i} + \alpha_{\text{sp},ii})}{M_{s,i}} \mathbf{M}_i \times \frac{d\mathbf{M}_i}{dt} - \frac{\alpha_{\text{sp},ij}}{M_{s,i}} \mathbf{M}_i \times \left(\mathbf{m}_j \times \frac{d\mathbf{m}_j}{dt} \right) \times \mathbf{M}_i \tag{2}$$

On the right-hand side of Eq. (2), the first term describes the precession with the effective field $\mathbf{H}_{\text{eff},i}$ in each layer, given by the partial derivative of the total free energy in the \mathbf{M} space via $\mathbf{H}_{\text{eff},i} = -\nabla_{\mathbf{M}_i} F$. The second term represents the relaxation induced by Gilbert damping (α) of the i -th layer, which includes the intrinsic ($\alpha_{0,i}$) and spin-pumping-enhanced ($\alpha_{\text{sp},ii}$) damping. For TR-MOKE measurements, $\alpha_{0,i}$ and $\alpha_{\text{sp},ii}$ are indistinguishable. Hence, we define $\alpha_i = \alpha_{0,i} + \alpha_{\text{sp},ii}$ to include both terms. The last term in Eq. (2) considers the influence of pumped spin currents from the layer j on the magnetization dynamics of the layer i .

The time evolution of \mathbf{M}_i can be obtained by solving the linearized Eq. (2). Details are provided in Note 1 of the SM [35]. The solutions to Eq. (2) in spherical coordinates are:

$$\begin{bmatrix} \theta_1(t) \\ \varphi_1(t) \\ \theta_2(t) \\ \varphi_2(t) \end{bmatrix} = \begin{bmatrix} \theta_{0,1} \\ \varphi_{0,1} \\ \theta_{0,2} \\ \varphi_{0,2} \end{bmatrix} + \begin{bmatrix} \Delta\theta_1(t) \\ \Delta\varphi_1(t) \\ \Delta\theta_2(t) \\ \Delta\varphi_2(t) \end{bmatrix} = \begin{bmatrix} \theta_{0,1} \\ \varphi_{0,1} \\ \theta_{0,2} \\ \varphi_{0,2} \end{bmatrix} + \begin{bmatrix} C_{\theta,1}^{\text{HF}} \\ C_{\varphi,1}^{\text{HF}} \\ C_{\theta,2}^{\text{HF}} \\ C_{\varphi,2}^{\text{HF}} \end{bmatrix} \exp(i\omega^{\text{HF}}t) + \begin{bmatrix} C_{\theta,1}^{\text{LF}} \\ C_{\varphi,1}^{\text{LF}} \\ C_{\theta,2}^{\text{LF}} \\ C_{\varphi,2}^{\text{LF}} \end{bmatrix} \exp(i\omega^{\text{LF}}t) \quad (3)$$

with $\Delta\theta_i$ and $\Delta\varphi_i$ representing the deviation angles of magnetization from its equilibrium direction along the polar and azimuthal directions. The last two terms are the linear combination of two eigen-solutions, denoted by superscripts HF (high-frequency mode) and LF (low-frequency mode). ω is the complex angular frequencies of two modes, with the real and imaginary parts representing the precession angular frequency ($f/2\pi$) and relaxation rate ($1/\tau$), respectively. For each mode, the complex prefactor vector $[C_{\theta,1}, C_{\varphi,1}, C_{\theta,2}, C_{\varphi,2}]^T$ contains detailed information about the magnetization dynamics. As illustrated in Fig. 1(c), the moduli, $|C_{\theta,i}|$ and $|C_{\varphi,i}|$ correspond to the half cone angles of the precession in layer i along the polar and azimuthal directions for a given mode immediately after laser heating, as shown by $\Delta\theta$ and $\Delta\varphi$ in Figs. 1(b-c). The phase difference between $\Delta\theta_i$ and $\Delta\varphi_i$, defined as $\text{Arg}(\Delta\theta_i/\Delta\varphi_i) = \text{Arg}(C_{\theta,i}/C_{\varphi,i})$ with Arg representing the argument of complex numbers, determines the direction of precession. If $\Delta\theta_i$ advances $\Delta\varphi_i$ by 90° , meaning $\text{Arg}(C_{\theta,i}/C_{\varphi,i}) = 90^\circ$, the precession is counter-clockwise (CCW) in the θ - φ space (from a view against \mathbf{M}_i). $\text{Arg}(C_{\theta,i}/C_{\varphi,i}) = -90^\circ$, on the contrary, suggests clockwise (CW) precession [Fig. 1(d)]. Further, the argument of $C_{\theta,2}/C_{\theta,1}$ provides the relative phase in two FM layers. $\text{Arg}(C_{\theta,2}/C_{\theta,1}) = 0^\circ$ corresponds to the precession motions in two FM layers that are in-phase (IP) in terms of θ for a given mode. While the out-of-phase (OOP) precession in terms of θ is represented by $\text{Arg}(C_{\theta,2}/C_{\theta,1}) = 180^\circ$ [Fig. 1(e)]. Given the precession

direction in each layer and the phase difference between the two FM layers in terms of θ , the phase difference in terms of φ can be automatically determined.

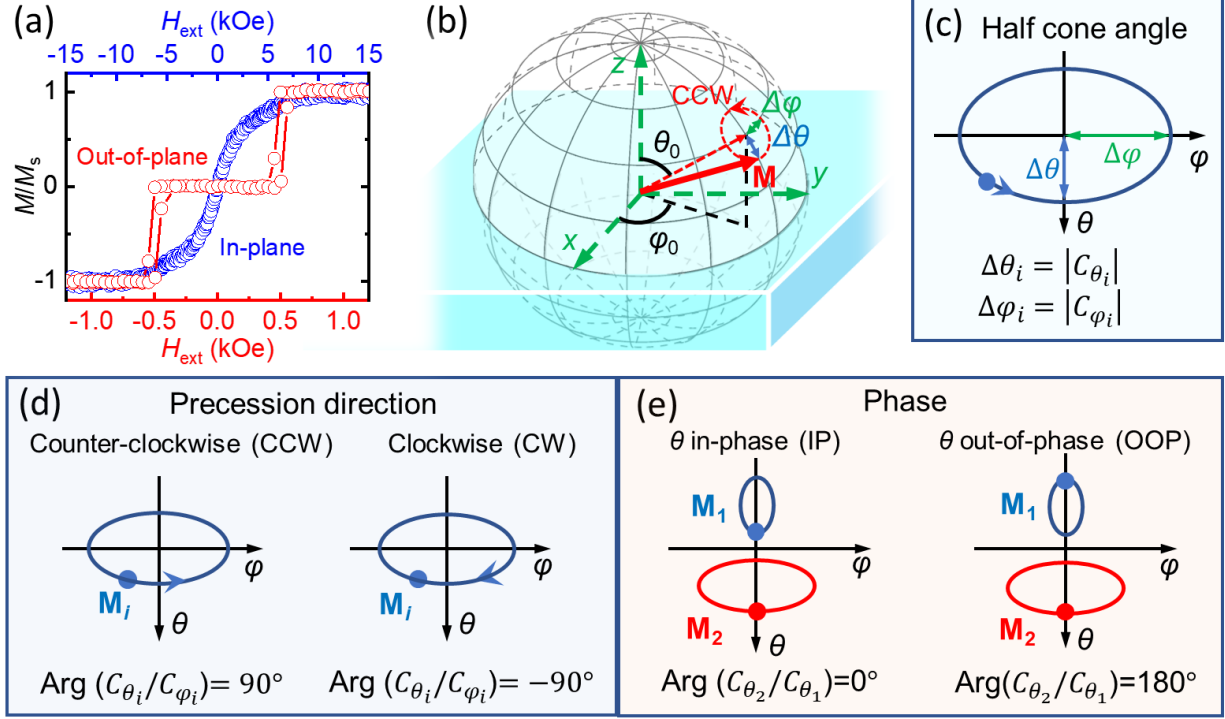


FIG. 1 (a) Magnetic hysteresis (M - H_{ext}) loops of the p-SAF stack. The magnetization is normalized to the saturation magnetization (M/M_s). (b) Schematic illustration of the half cone angles ($\Delta\theta$ and $\Delta\varphi$) and precession direction of magnetization. The precession direction is defined from a view against the equilibrium direction (θ_0 , φ_0) of \mathbf{M} . The representative precession direction in the schematic is counterclockwise (CCW). (c) The relation between precession half cone angles and the prefactors. (d) The relation between precession direction and the prefactors. (e) The relative phase between two FM layers for different prefactor values.

As for the effective damping $\alpha_{eff} = 1/2\pi f\tau$, in addition to the intrinsic damping ($\alpha_{0,i}$) and the spin-pumping contribution ($\alpha_{sp,ii}$ and $\alpha_{sp,ji}$) considered in Eq. (2), inhomogeneities can also bring substantial damping enhancement [32,33,41,42]. Here, we model the total relaxation rate as follows:

$$\frac{1}{\tau^\Phi} = -\text{Im}(\omega^\Phi) + \frac{1}{\tau_{\text{inhomo}}^\Phi} \quad (4)$$

The superscript $\Phi = \text{HF}$ or LF , representing either the high-frequency or low-frequency precession modes. ω^Φ includes both the intrinsic and spin-pumping contributions. The inhomogeneous broadening is calculated as:

$$\frac{1}{\tau_{\text{inhomo}}^\Phi} = \sum_i \frac{1}{\pi} \left| \frac{\partial f^\Phi}{\partial H_{k,\text{eff},i}} \right| \Delta H_{k,\text{eff},i} + \sum_i \frac{1}{\pi} \left| \frac{\partial f^\Phi}{\partial J_i} \right| \Delta J_i \quad (5)$$

where the first summation represents the contribution from the spatial variation of the effective anisotropy field of individual FM layers ($\Delta H_{k,\text{eff},i}$). The second summation denotes the contribution from the spatial fluctuations of the bilinear and biquadratic IEC (ΔJ_1 and ΔJ_2). According to Slonczewski's "thickness fluctuations" theory, ΔJ_1 generates J_2 [43,44]. Therefore, the fact that $J_2 = 0$ for our sample suggests that ΔJ_1 is sufficiently small, allowing us to neglect the inhomogeneous broadening from the fluctuations of both the bilinear and biquadratic IEC in the following analyses.

2.3 Detection of magnetization dynamics

The magnetization dynamics of the p-SAF sample is detected by TR-MOKE, which is ultrafast-laser-based metrology utilizing a pump-probe configuration. In TR-MOKE, pump laser pulses interact with the sample, initiating magnetization dynamics in magnetic layers via inducing ultrafast thermal demagnetization. The laser-induced heating brings a rapid decrease to the magnetic anisotropy fields and IEC [45,46], which changes $\theta_{0,i}$, $\varphi_{0,i}$ and initiates the precession. The magnetization dynamics due to pump excitation is detected by a probe beam through the magneto-optical Kerr effect. In our setup, the incident probe beam is normal to the sample surface (polar MOKE); therefore, the Kerr rotation angle (θ_K) of the reflected probe beam is proportional to the z component of the magnetization [47]. More details about the experimental setup can be

found in Refs. [30,32]. For p-SAF, TR-MOKE signals contain two oscillating frequencies that correspond to the HF and LF modes ($f^{\text{HF}} > f^{\text{LF}}$). The signals are proportional to the change in θ_K and can be analyzed as follows:

$$\Delta\theta_K(t) = A + Be^{-t/\tau^T} + C^{\text{HF}}\cos(2\pi f^{\text{HF}}t + \beta^{\text{HF}})e^{-t/\tau^{\text{HF}}} + C^{\text{LF}}\cos(2\pi f^{\text{LF}}t + \beta^{\text{LF}})e^{-t/\tau} \quad (6)$$

where the exponential term Be^{-t/τ^T} is related to the thermal background with τ^T being the time scale of heat dissipation. The rest two terms on the right-hand side are the precession terms with $C, f, \beta,$ and τ denoting, respectively, the amplitude, frequency, phase, and relaxation time of the HF and LF modes.

After excluding the thermal background from TR-MOKE signals, the precession is modeled with the initial conditions of step-function decreases in $H_{k,\text{eff},i}$ and J_i , following the ultrafast laser excitation [48]. This is a reasonable approximation since the precession period ($\sim 15\text{-}100$ ps for $H_{\text{ext}} > 5$ kOe) is much longer than the time scales of the laser excitation (~ 1.5 ps) and subsequent relaxations among electrons, magnons, and lattice ($\sim 1\text{-}2$ ps) [49], but much shorter than the time scale of heat dissipation-governed recovery (~ 400 ps). With these initial conditions, the prefactors in Eq. (3) can be determined (see more details in Note 1 of the SM [35]).

For our SAF structure, θ_K detected by the probe beam contains weighted contributions from both the top and bottom FM layers:

$$\frac{\theta_K(t)}{\theta_{K,s}} = w\cos\theta_1(t) + (1 - w)\cos\theta_2(t) \quad (7)$$

where $\theta_{K,s}$ represents the Kerr rotation angle when the SAF stack is saturated along the positive out-of-plane (z) direction. w is the weighting factor, considering the different contributions to the total MOKE signals from two FM layers. w can be obtained from static MOKE measurements [50], which gives $w = 0.457$ (see more details in Note 2 of the SM [35]).

3 RESULTS AND DISCUSSION

3.1 Field-dependent precession frequencies and equilibrium magnetization directions

TR-MOKE signals measured at varying H_{ext} are depicted in Fig. 2(a). The external field is tilted 15° away from in-plane [$\theta_H = 75^\circ$, as defined by Fig. 2(c)] to achieve larger amplitudes of TR-MOKE signals [51]. The signals can be fitted to Eq. (6) to extract the LF and HF precession modes. The field-dependent precession frequencies of both modes are summarized in Fig. 2(b). For simplicity, when analyzing precession frequencies, magnetic damping and mutual spin pumping are neglected due to its insignificant impacts on precession frequencies. By comparing the experimental data and the prediction of $\omega^{\text{HF}}/2\pi$ and $\omega^{\text{LF}}/2\pi$ based on Eq. (3), the effective anisotropy fields and the IEC strength are fitted as $H_{\text{k,eff},1} = 1.23 \pm 0.28$ kOe, $H_{\text{k,eff},2} = 6.18 \pm 0.13$ kOe, $J_1 = -0.050 \pm 0.020$ erg cm^{-2} , and $J_2 = 0$. All parameters and their determination methods are summarized in Table SI of the SM [35]. The fitted J_1 is close to that obtained from the M - H_{ext} loops (~ -0.062 erg cm^{-2}). The inset of Fig 2(b) shows the zoomed-in view of field-dependent precession frequencies around $H_{\text{ext}} = 8$ kOe, where an anti-crossing feature is observed: a narrow gap (~ 2 GHz) opens in the frequency dispersion curves of the HF and LF modes owing to the weak IEC between two FM layers. Without any IEC, the precession frequencies of two FM layers would cross at $H_{\text{ext}} = 8$ kOe, as indicated by the green dashed line and blue dashed line in the figure. We refer to these two sets of crossing frequencies as the single-layer natural frequencies of two FM layers (FM₁ and FM₂) in the following discussions.

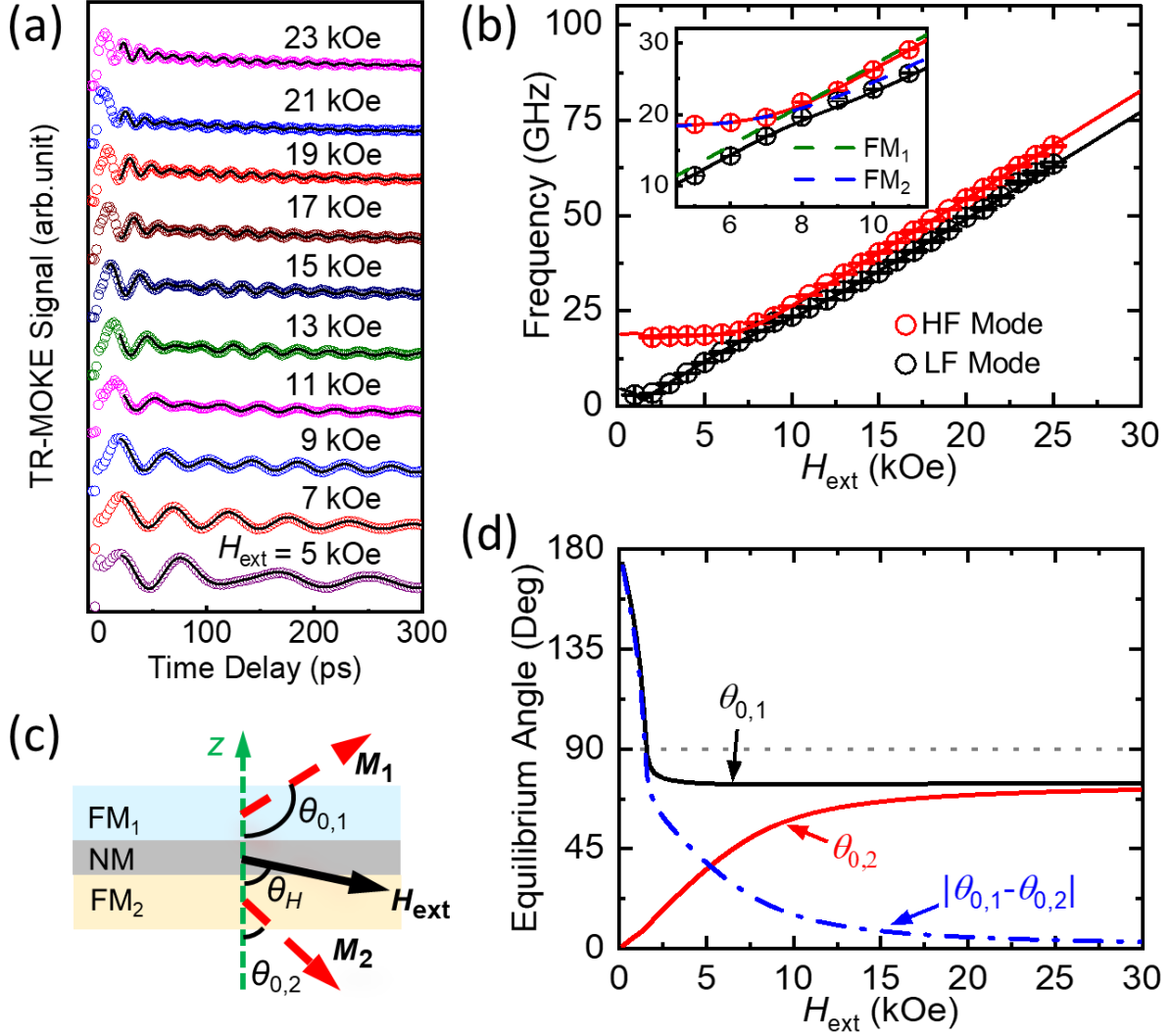


FIG. 2 (a) TR-MOKE signals under varying H_{ext} when $\theta_H = 75^\circ$ [as defined in panel (c)]. Circles are the experimental data and black lines are the fitting curves based on Eq. (6). (b) The precession frequencies of the HF and LF modes as functions of H_{ext} . Circles are experimental data and solid lines are fitting curves. The inset highlights the zoomed-in view of the field-dependent frequencies around 8 kOe, where the green dashed line and blue dashed line are the single-layer (SL) precession frequencies of FM₁ and FM₂ without interlayer exchange coupling. (c) Schematic illustration of the definition of the equilibrium polar angles ($\theta_{0,1}$ and $\theta_{0,2}$), and the direction of the external magnetic field (θ_H). The illustration is equivalent to Fig. 1(b) due to symmetry. (d) $\theta_{0,1}$ and $\theta_{0,2}$ as functions of H_{ext} . The dash-dotted line plots the difference between the two equilibrium polar angles.

Based on the fitted stack properties ($H_{k,\text{eff},1}$, $H_{k,\text{eff},2}$, J_1 , and J_2), the equilibrium magnetization directions in the two layers can be calculated. For SAFs with weak IEC compared with uniaxial PMA, the azimuthal angles of the magnetization in two FM layers are always the same as that of the external field at equilibrium status. Therefore, two polar angles will be sufficient to describe the equilibrium magnetization configuration. Figure 2(c) illustrates the definition of the equilibrium polar angles of two FM layers ($\theta_{0,1}$, $\theta_{0,2}$) and the external field (θ_H). The values of $\theta_{0,1}$, $\theta_{0,2}$, and the difference between these two polar angles as functions of H_{ext} are shown in Fig. 2(d). When H_{ext} is low (< 1.6 kOe), magnetic anisotropy and antiferromagnetic coupling are dominant and $|\theta_{0,1} - \theta_{0,2}|$ is larger than 90° . As H_{ext} increases, both $\theta_{0,1}$ and $\theta_{0,2}$ approach θ_H . When H_{ext} is high (> 15 kOe), the Zeeman energy becomes dominant and both M_1 and M_2 are almost aligned with H_{ext} .

3.2 Cone angle, direction, and phase of magnetization precession revealed by modeling

Besides the equilibrium configuration, using sample properties extracted from Fig. 2(b) as input parameters, the LLG-based modeling (described in section 2.2) also provides information on the cone angle, direction, and phase of magnetization precession for each mode (Fig. 1). The discussion in this section is limited to the case without damping and mutual spin pumping. They will be considered in Note 4 of the SM [35], sections 3.3, and 3.4. The calculation results are shown in Fig. 3, which are categorized into three regions. At high external fields ($H_{\text{ext}} > 1.6$ kOe, regions 2 and 3), both FM layers precess CCW [$\text{Arg}(C_{\theta,i}/C_{\varphi,i}) = 90^\circ$], and the polar angles of magnetization in two layers are in-phase [$\text{Arg}(C_{\theta,2}/C_{\theta,1}) = 0^\circ$] for the HF mode and out-of-phase [$\text{Arg}(C_{\theta,2}/C_{\theta,1}) = 180^\circ$] for the LF mode. This is the reason for the HF mode (LF mode) also being called the acoustic mode (optical mode) in the literature [23]. The criterion to differentiate

region 2 from region 3 is the FM layer that dominates a given precessional mode (*i.e.*, the layer with larger precession cone angles). In region 2 ($1.6 \text{ kOe} < H_{\text{ext}} < 8 \text{ kOe}$), the HF mode is dominated by FM₂ because FM₂ has larger cone angles than FM₁. This is reasonable since the higher precession frequency is closer to the natural frequency of FM₂ [see Fig. 2(b)] in region 2. Similarly, in region 3, the HF mode is dominated by FM₁ with larger precession cone angles.

When H_{ext} is low (region 1), the angle between two magnetizations is larger than 90° [Fig. 2(d)] owing to the more dominant AF-exchange-coupling energy as compared with the Zeeman energy. In this region, magnetization dynamics exhibits some unique features. Firstly, CW [$\text{Arg}(C_{\theta,i}/C_{\varphi,i}) = -90^\circ$] precession emerges: for each mode, the dominant layer precesses CCW (FM₂ for the HF mode and FM₁ for the LF mode) and the subservient layer precesses CW (FM₁ for the HF mode and FM₂ for the LF mode). This is because the effective field for the subservient layer [*e.g.*, $\mathbf{H}_{\text{eff},1}$ for the HF mode, see Eq. (2)] precesses CW owing to the CCW precession of the dominant layer when $|\theta_{0,1} - \theta_{0,2}| > 90^\circ$ [Fig. 2(d)]. In other words, a low H_{ext} that makes $|\theta_{0,1} - \theta_{0,2}| > 90^\circ$ is a necessary condition for the CW precession. However, it is not a sufficient condition. In general, certain degrees of symmetry breaking ($H_{k,\text{eff},1} \neq H_{k,\text{eff},2}$ or the field is tilted away from the direction normal to the easy axis) are also needed to generate CW precession. For example, for symmetric antiferromagnets ($H_{k,\text{eff},1} = H_{k,\text{eff},2}$) under fields perpendicular to the easy axis, CW precession does not appear even at low fields (Fig. 2(a) in Ref. [52]). See Note 5 of the SM [35] for more details. Secondly, as shown in Fig. 3, the precession motions in two FM layers are always in-phase for both HF and LF modes; thus, there is no longer a clear differentiation between “acoustic mode” and “optical mode”. Instead, the two modes can be differentiated as “right-handed” and “left-handed” based on the chirality [53]. Here, we define the chirality with respect to a reference direction taken as the projection of \mathbf{H}_{ext} or \mathbf{M}_2 (magnetization direction of the layer with

a higher $H_{k,\text{eff}}$ on the easy axis [-z direction in Fig. 3(c)]. Lastly, the shape of the precession cone also varies in different regions. $\Delta\theta_i$ and $\Delta\varphi_i$ are almost the same for both modes in region 3, indicating the precession trajectories are nearly circular. While in regions 1 and 2, $\Delta\theta_i$ and $\Delta\varphi_i$ are not always equal, suggesting the precession trajectories may have high ellipticities.

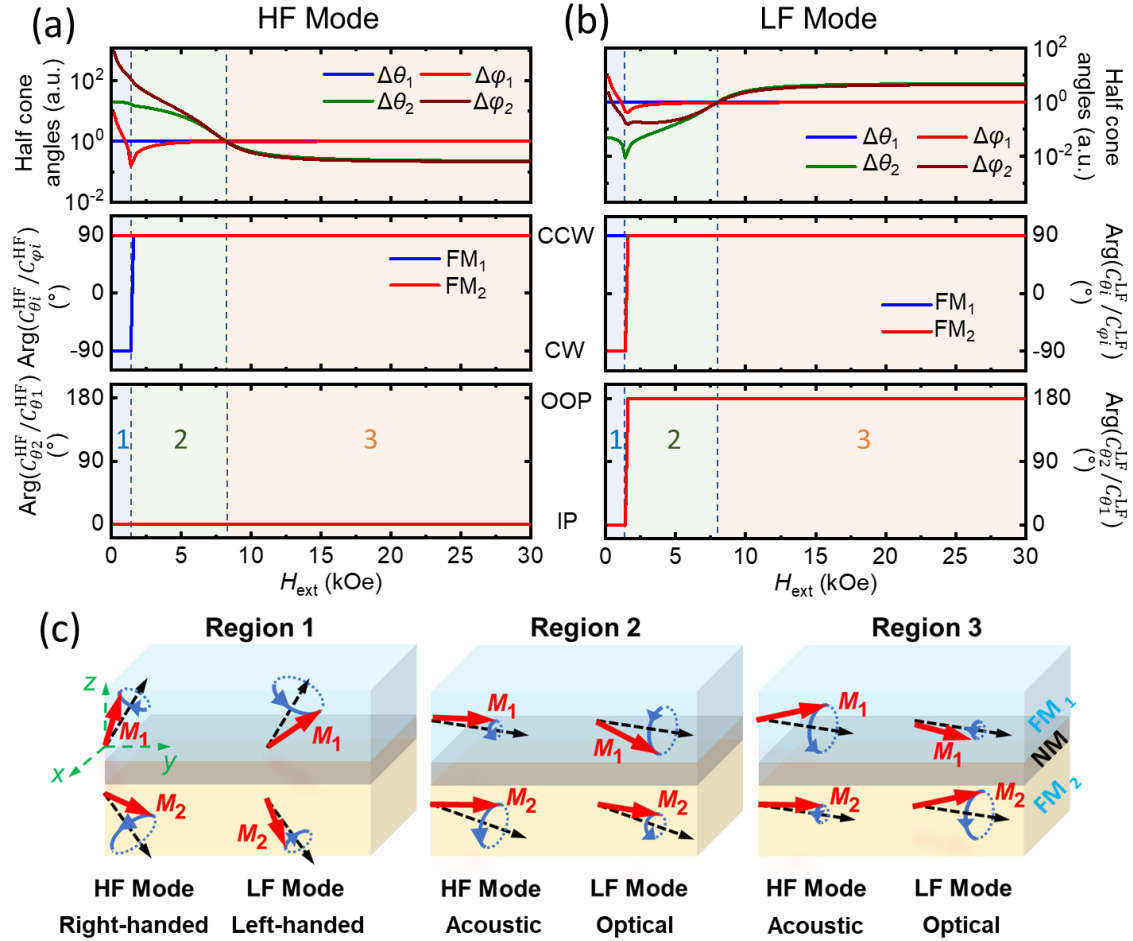


FIG. 3 The calculated half cone angle, direction, and phase of magnetization precession for (a) the HF mode and (b) the LF mode. In the top row, four curves represent the polar and azimuthal half cone angles of precession in two FM layers. All half cone angles are normalized with respect to $\Delta\theta_1$. The middle row shows the value of $\text{Arg}(C_{\theta,i}/C_{\varphi,i})$ under different H_{ext} . A value of 90° (-90°) represents CCW (CW) precession. The bottom row is the phase difference of the polar angles in two layers. A value of 0° (180°) corresponds to the polar angles of the magnetization in two layers are IP (OOP) during precession. Dashed lines correspond to the reference case where damping is zero in both layers. (c) Schematic illustrations of the cone angle, direction, and phase of

magnetization precession for the HF and LF modes in different regions, and their corresponding characteristics regarding chirality and phase difference.

3.3 Amplitude and phase of TR-MOKE signals

Actual magnetization dynamics is resolvable as a linear combination of the two eigenmodes (the HF and the LF modes). By taking into account the initial conditions (*i.e.*, laser excitation, see Note 1 of the SM [35]), we can determine the amplitude and phase of the two modes in TR-MOKE signals. Figure 4(a) summarizes the amplitudes of both HF and LF modes [C^{HF} and C^{LF} in Eq. (3)] under different H_{ext} . Noted that the y-axis represents Kerr angle (θ_{K}) instead of the cone angle of precession. The LF mode has a local minimum near 8 kOe, where the two FM layers have similar precession cone angles but opposite phases for the LF mode [Fig. 3(b)]. The amplitudes of both modes decrease with H_{ext} in the high-field region. This is similar to the single-layer case, where the amplitudes of TR-MOKE signals decrease with H_{ext} because the decrease in $H_{\text{k,eff}}$ induced by laser heating is not able to significantly alternate the equilibrium magnetization direction when the Zeeman energy dominates [51]. The LF mode also has an amplitude peak at low fields ($H_{\text{ext}} < 3$ kOe), where the dominant layer of FM₁ changes its equilibrium direction dramatically with H_{ext} (from $\sim 75^\circ$ to 170°) as shown in Fig. 2(d).

To directly compare the amplitudes of TR-MOKE signals and the LLG-based calculations, the weighting factor w and the initial conditions are needed. The initial conditions are determined by $H'_{\text{k,eff,1}}$, $H'_{\text{k,eff,2}}$, and J'_1 , representing the instantaneous effective anisotropy fields and IEC strength upon laser heating. These instantaneous properties are different from their corresponding room-temperature values ($H_{\text{k,eff,1}}$, $H_{\text{k,eff,2}}$, and J_1). The accurate determination of $H'_{\text{k,eff,1}}$, $H'_{\text{k,eff,2}}$, and J'_1 demands the modeling of the laser heating process as well as the temperature dependence of stack properties, which are challenging. Here, we treat these three variables as adjustable parameters and

determine their values by fitting the field-dependent amplitudes of TR-MOKE signals, which yields $H'_{k,\text{eff},1}/H_{k,\text{eff},1} = 0.90 \pm 0.01$, $H'_{k,\text{eff},2}/H_{k,\text{eff},2} = 0.95 \pm 0.01$, and $J'_1/J_1 = 0.83 \pm 0.01$. It is apparent that the field dependence of TR-MOKE signal amplitude is in excellent agreement with the theoretical modeling, as shown in Fig. 4(a).

Figure 4(b) shows the calculated half polar cone angles for each mode in each FM layer. In TR-MOKE signals, the optical mode (the LF mode in regions 2 and 3) tends to be partially canceled out because the two layers precess out-of-phase. Therefore, compared with Fig. 4(a), the information in Fig. 4(b) better reflects the actual intensity of both modes in FM₁ and FM₂. In Fig. 4(b), the precession cone angles of both modes in FM₁ ($\Delta\theta_1^{\text{HF}}$, $\Delta\theta_1^{\text{LF}}$) have local maxima at the anti-crossing field ($H_{\text{ext}} \approx 8$ kOe). On the contrary, $\Delta\theta_2^{\text{LF}}$ and $\Delta\theta_2^{\text{HF}}$ of FM₂ have their maxima either above or below the anti-crossing field. This is because FM₂ has larger precession amplitudes (cone angles) than FM₁ at the anti-crossing field if there is no IEC [the dotted lines of FM₁ (SL) and FM₂ (SL) in Fig. 4(b)]. With IEC, FM₂ with larger cone angles can drive the precession motion in FM₁ significantly near the anti-crossing field, where IEC is effective. Subsequently, the precession amplitudes of FM₁ exhibit local maxima as its cone angle peaks at the anti-crossing field [solid lines in Fig. 4(b)]. Also, compared with the uncoupled case [FM₁ (SL) in Fig. 4(b)], FM₁ in the SAF structure has a much larger cone angle at the boundary between regions 1 and 2 ($H_{\text{ext}} \approx 1.6$ kOe). This corresponds to the case where FM₁ fast switching is driven by H_{ext} , as shown in Fig. 2(d). The energy valley of FM₁ created by IEC and uniaxial anisotropy is canceled out by H_{ext} . As a result, any perturbation in $H_{k,\text{eff},1}$ or IEC can induce a large change in θ_1 .

Besides amplitude, the phase of TR-MOKE signals [β^{HF} and β^{LF} in Eq. (6)] also provides important information about the magnetization dynamics in SAF [Fig. 4(c)]. In Fig. 4(c), the phase of the HF mode stays constant around π . However, the LF mode goes through a π -phase shift at

the transition from region 2 to region 3. This phase shift can be explained by the change of the dominant layer from region 2 to region 3 for the LF mode [Fig. 3(c)]. As illustrated in Fig. 4(d), the LF mode (optical mode in regions 2 and 3) has opposite phases in FM₁ (~0°) and FM₂ (~180°). Considering the two FM layers have comparable optical contributions to TR-MOKE signals ($w \approx 0.5$), TR-MOKE signals will reflect the phase of the dominant layer for each mode. In region 3, FM₂ has larger precession cone angles than FM₁ for the LF mode; therefore, LF TR-MOKE signals have the same phase as FM₂ (~180°). However, in region 2, the dominant layer shifts from FM₂ to FM₁ for the LF mode. Hence, the phase of LF TR-MOKE signals also changes by ~180° to be consistent with the phase of FM₁ (~0°). As for the HF mode, since the two layers always have almost the same phase (~180°), the change of the dominant layer does not cause a shift in the phase of TR-MOKE signals.

By comparing Fig. 4(d) and Fig. 3(a-b), one can notice that the phase difference between two FM layers could deviate from 0° or 180° when damping and mutual spin pumping is considered [Fig. 4(d)]. The deviation of phase allows energy to be transferred from one FM layer to the other during precession via exchange coupling [54]. In our sample system, FM₂ has a higher damping constant ($\alpha_1 = 0.020$ and $\alpha_2 = 0.060$); therefore, the net transfer of energy is from FM₁ to FM₂. More details can be found in Note 4 of the SM [35], which shows the phase of TR-MOKE signals is affected by Gilbert damping in both layers and the mutual spin pumping. By fitting the phase [Fig. 4(c)] and the damping [Fig. 5(a)] of TR-MOKE signals simultaneously, we obtained $\alpha_{sp,12} = 0.010 \pm 0.004$, $\alpha_{sp,21} = 0.007^{+0.009}_{-0.007}$, $\alpha_1 = 0.020 \pm 0.002$, and $\alpha_2 = 0.060 \pm 0.008$. Nonreciprocal spin pumping damping ($\alpha_{sp,12} \neq \alpha_{sp,21}$) has been reported in asymmetric FM₁/NM/FM₂ trilayers and attributed to the different spin-mixing conductance ($g_i^{\uparrow\downarrow}$) at the two FM/NM interfaces [27], following $\alpha_{sp,ij} = g_i \mu_B g_j^{\uparrow\downarrow} / (8\pi M_{s,i} d_i)$, with g_i the g -factor of the i -th layer and μ_B the Bohr

magneton [55]. The above equation neglects the spin-flip scattering in NM and assumes that the spin accumulation in the NM spacer equally flows back to FM₁ and FM₂ [37]. However, the uncertainties of our $\alpha_{\text{sp},ij}$ are too high to justify the nonreciprocity of $\alpha_{\text{sp},ij}$ (see Note 3 of the SM [35] for detailed uncertainty analyses). In fact, if the spin backflow to FM_{*i*} is proportional to $g_i^{\uparrow\downarrow}$, then $\alpha_{\text{sp},ij} = g_i \mu_B g_i^{\uparrow\downarrow} g_j^{\uparrow\downarrow} / [4\pi M_{s,i} d_i (g_i^{\uparrow\downarrow} + g_j^{\uparrow\downarrow})]$ (Eq. 1.14 in Ref.[56]). In this case, the different spin-mixing conductance at two FM/NM interfaces ($g_1^{\uparrow\downarrow} \neq g_2^{\uparrow\downarrow}$) will not lead to nonreciprocal $\alpha_{\text{sp},ij}$. Although differences in g_i and magnetic moment per area ($M_{s,i} d_i$) can potentially lead to nonreciprocal $\alpha_{\text{sp},ij}$, the values of g_i and $M_{s,i} d_i$ for the two FM layers are expected to be similar (the net magnetization of SAF is zero without external fields). Therefore, nearly reciprocal $\alpha_{\text{sp},ij}$ are plausible for our SAF stack. Assuming $g_i^{\uparrow\downarrow}$ values are similar at the two FM/NM interfaces ($g_1^{\uparrow\downarrow} \approx g_2^{\uparrow\downarrow} = g^{\uparrow\downarrow}$), this yields $g^{\uparrow\downarrow} = 8\pi M_{s,i} d_i \alpha_{\text{sp},ij} / (g_i \mu_B) = 1.2 \sim 1.7 \times 10^{15} \text{ cm}^{-2}$. $g^{\uparrow\downarrow}$ can also be estimated from the free electron density per spin (n) in the NM layer: $g^{\uparrow\downarrow} \approx 1.2n^{2/3}$ [57]. With $n = 5.2 \times 10^{28} \text{ m}^{-3}$ for Ru [58] (the value of n is similar for Ta [59]), $g^{\uparrow\downarrow}$ is estimated to be $1.7 \times 10^{15} \text{ cm}^{-2}$, the same order as the $g^{\uparrow\downarrow}$ value from TR-MOKE measurements, which justifies the $\alpha_{\text{sp},ij}$ values derived from TR-MOKE are within a reasonable range. The values of α_1 and α_2 will be discussed in section 3.4.

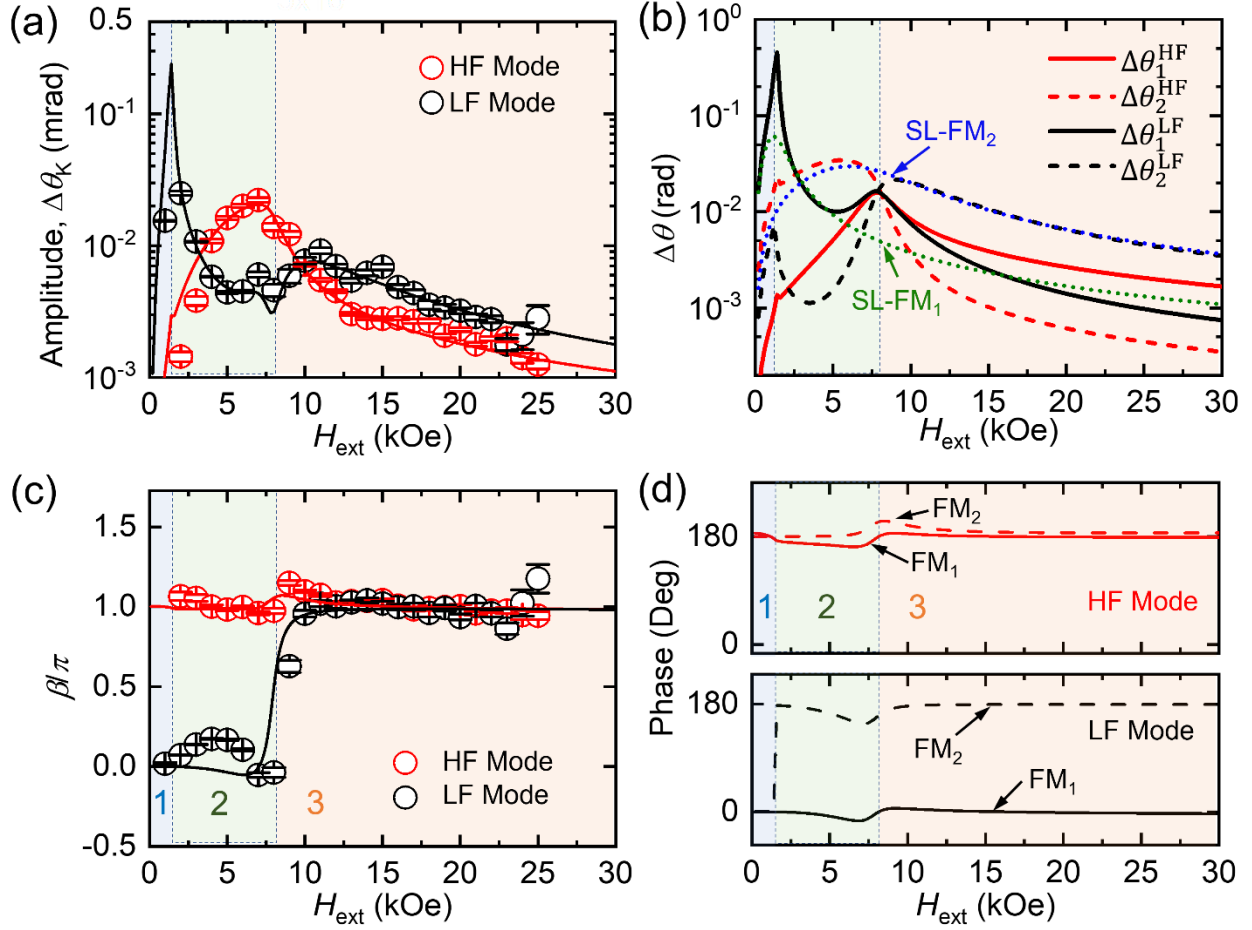


FIG. 4 (a) Amplitudes of TR-MOKE signals as functions of H_{ext} . The circles and curves represent experimental data and modeling fitting, respectively. (b) The calculated precession half cone angles at different H_{ext} . Red curves and black curves represent the cone angles of the HF mode and the LF mode in FM₁ (solid lines) and FM₂ (dashed lines). Dotted lines are the precession cone angles of single-layer (SL) FM₁ and FM₂ without IEC. (c) Phases of TR-MOKE signals at varying H_{ext} . Circles and curves are experimental data and modeling fitting ($\alpha_{\text{sp},12} = 0.010$, $\alpha_{\text{sp},21} = 0.007$, $\alpha_1 = 0.020$, $\alpha_2 = 0.060$). (d) Simulated precession phase of the HF mode (red curves) and the LF mode (black curves) in FM₁ (solid lines) and FM₂ (dashed lines).

3.4 Magnetic damping of the HF and LF precession modes

In addition to the amplitude and phase of TR-MOKE signals for the p-SAF stack, the model analyses also provide a better understanding of magnetic damping. Figure 5(a) shows the effective damping constant ($\alpha_{\text{eff}} = 1/2\pi f\tau$) measured at different H_{ext} (symbols), in comparison with

modeling fitting (solid lines). The general H_{ext} dependence of α_{eff} can be well captured by the model. The fitted Gilbert damping, $\alpha_1 = 0.020 \pm 0.002$ and $\alpha_2 = 0.060 \pm 0.008$ are close to the Gilbert damping of Ta/CoFeB(1 nm)/MgO thin films (~ 0.017) [41,60] and Co/Pd multilayers with a similar $t_{\text{Co}}/t_{\text{Pd}}$ ratio (~ 0.085) [61]. Other fitted parameters are $\Delta H_{\text{k,eff},1} = 0.26 \pm 0.02$ kOe, $\Delta H_{\text{k,eff},2} = 1.42 \pm 0.18$ kOe, $\alpha_{12}^{\text{sp}} = 0.010 \pm 0.004$, $\alpha_{21}^{\text{sp}} = 0.007_{-0.007}^{+0.009}$. ΔJ_1 and ΔJ_2 are set to be zero, as explained in Sec. 2.2. More details regarding the values and determination methods of all parameters involved in our data reduction are provided in Note 3 of the SM [35]. Dashed lines show the calculated α_{eff} without inhomogeneous broadening. At high H_{ext} , the difference between the solid lines and dashed lines approaches zero because the inhomogeneous broadening is suppressed. At low H_{ext} , the solid lines are significantly higher than the dashed lines, indicating substantial inhomogeneous broadening contributions.

The effective damping shows interesting features near the anti-crossing field. As shown in Fig. 5(b), due to the effective coupling between two FM layers near the anti-crossing field, the hybridization of precession in two FM layers leads to a mix of damping with contributions from both layers. The effective damping of the FM₁-dominant mode reaches a maximum within the anti-crossing region ($7 \leq H_{\text{ext}} \leq 10$ kOe) and is higher than the single-layer (SL) FM₁ case. Similarly, the hybridized HF and LF modes at 8.5 kOe exhibit a lower α_{eff} (~ 0.073) compared to the SL FM₂ case. α_{eff} consists of contributions from Gilbert damping (α_i), mutual spin pumping ($\alpha_{\text{sp},ij}$, $i \neq j$), and inhomogeneous broadening ($\Delta H_{\text{k,eff},i}$ and ΔJ_i). To better understand the mixing damping behavior, Fig. 5(c) shows α_{eff} after excluding the inhomogeneous contribution ($\alpha_{\text{eff}}^{\text{inhomo}}$). Compared to the SL layer case (green and blue dashed lines), the HF and LF modes (red and black dashed lines) clearly suggest that IEC effectively mixes the damping in two layers around the anti-crossing field. Without the IEC, precession in FM₂ with a higher damping relaxes faster than that

in FM₁. However, the IEC provides a channel to transfer energy from FM₁ to FM₂, such that the two layers have the same precession relaxation rate for a given mode. Near the anti-crossing field, two layers have comparable precession cone angles; therefore, the damping values of the hybridized modes are roughly the average of two FM layers. In addition to the static IEC, dynamic spin pumping can also modify the damping of individual modes. The black and red solid lines represent the cases with mutual spin pumping ($\alpha_{sp,12} = 0.01$ and $\alpha_{sp,21} = 0.007$). Generally, in regions 2 & 3, mutual spin pumping reduces the damping of the HF mode and increases the damping of the LF mode because the HF (LF) mode is near in-phase (out-of-phase). Overall, the static IEC still plays the essential role for the damping mix near the anti-crossing field.

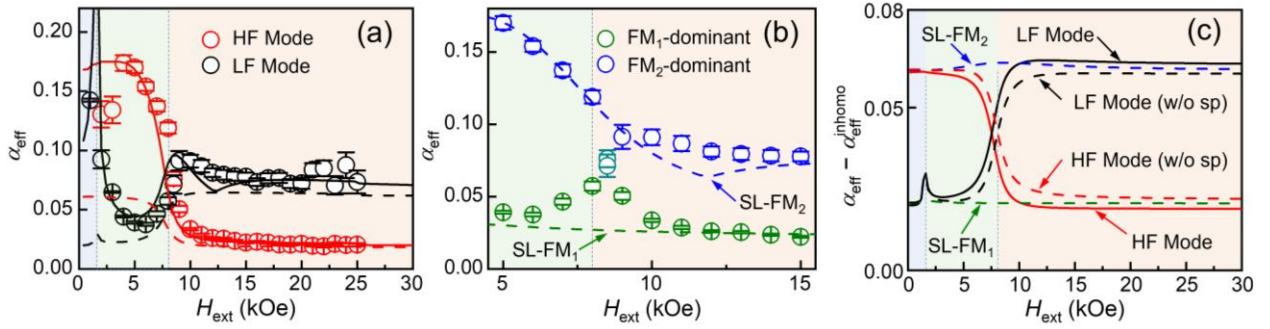


FIG. 5 (a) Effective damping constant under varying H_{ext} . Circles are experimental data. Solid lines are fitting curves based on Eqs. (4-5). Dashed lines denote α_{eff} after the removal of inhomogeneous-broadening contribution. (b) A zoomed-in figure of panel (a) between 5 kOe and 15 kOe. Blue and green circles are measured effective damping of the mode dominated by FM₁ and FM₂, respectively. Blue and green dashed lines are the α_{eff} of FM₁ and FM₂ single layer without IEC. (c) Effective damping after excluding the inhomogeneous contribution as a function of H_{ext} . The HF mode (red curves) and the LF mode (black curves) are represented by solid (or dashed) curves when the mutual spin pumping terms ($\alpha_{sp,12}$ and $\alpha_{sp,21}$) are considered (or excluded). The dashed green and blue lines are the SL cases for FM₁ and FM₂, respectively.

4 CONCLUSION

We systematically investigated the magnetization dynamics excited by ultrafast laser pulses in an asymmetric p-SAF sample both theoretically and experimentally. We obtained detailed information regarding magnetization dynamics, including the cone angles, directions, and phases of spin precession in each layer under different H_{ext} . In particular, the dynamic features in the low-field region (region 1) exhibiting CW precession, were revealed. The resonance between the precession of two FM layers occurs at the boundary between regions 2 and 3, where an anti-crossing feature is present in the frequency *vs.* H_{ext} profile. The dominant FM layer for a given precession mode also switches from region 2 to region 3. The amplitude and phase of TR-MOKE signals are well captured by theoretical modeling. Importantly, we successfully quantified the individual contributions from various sources to the effective damping, which enables the determination of Gilbert damping for both FM layers. At low H_{ext} , the contribution of inhomogeneous broadening to the effective damping is significant. Near the anti-crossing field, the effective damping of two coupled modes contains substantial contributions from both FM layers owing to the strong hybridization via IEC. Although the analyses were made for an asymmetric SAF sample, this approach can be directly applied to study magnetization dynamics and magnetic properties of general complex material systems with coupled multilayers, and thus benefits the design and optimization of spintronic materials via structural engineering.

Acknowledgements

This work is primarily supported by the National Science Foundation (NSF, CBET- 2226579). D.L.Z gratefully acknowledges the funding support from the ERI program (FRANC) “Advanced MTJs for computation in and near random access memory” by DARPA, and ASCENT, one of six

centers in JUMP (a Semiconductor Research Corporation program, sponsored by MARCO and DARPA). J.P.W and X.J.W also appreciate the partial support from the UMN MRSEC Seed program (NSF, DMR-2011401). D.B.H. would like to thank the support from the UMN 2022-2023 Doctoral Dissertation Fellowship. The authors appreciated the valuable discussion with Prof. Paul Crowell.

References

- [1] R. Chen, Q. Cui, L. Liao, Y. Zhu, R. Zhang, H. Bai, Y. Zhou, G. Xing, F. Pan, H. Yang *et al.*, Reducing Dzyaloshinskii-Moriya interaction and field-free spin-orbit torque switching in synthetic antiferromagnets, *Nat. Commun.* **12**, 3113 (2021).
- [2] W. Legrand, D. Maccariello, F. Ajejas, S. Collin, A. Vecchiola, K. Bouzehouane, N. Reyren, V. Cros, and A. Fert, Room-temperature stabilization of antiferromagnetic skyrmions in synthetic antiferromagnets, *Nat. Mater.* **19**, 34 (2020).
- [3] D.-L. Zhang, C. Sun, Y. Lv, K. B. Schliep, Z. Zhao, J.-Y. Chen, P. M. Voyles, and J.-P. Wang, $L1_0$ Fe-Pd synthetic antiferromagnet through an fcc Ru spacer utilized for perpendicular magnetic tunnel junctions, *Phys. Rev. Appl.* **9**, 044028 (2018).
- [4] D.-S. Han, K. Lee, J.-P. Hanke, Y. Mokrousov, K.-W. Kim, W. Yoo, Y. L. W. van Hees, T.-W. Kim, R. Lavrijsen, C.-Y. You *et al.*, Long-range chiral exchange interaction in synthetic antiferromagnets, *Nat. Mater.* **18**, 703 (2019).
- [5] S.-H. Yang, K.-S. Ryu, and S. Parkin, Domain-wall velocities of up to 750 m s^{-1} driven by exchange-coupling torque in synthetic antiferromagnets, *Nat. Nanotechnol.* **10**, 221 (2015).
- [6] A. Fernández-Pacheco, E. Vedmedenko, F. Ummelen, R. Mansell, D. Petit, and R. P. Cowburn, Symmetry-breaking interlayer Dzyaloshinskii–Moriya interactions in synthetic antiferromagnets, *Nat. Mater.* **18**, 679 (2019).
- [7] T. Moriyama, W. Zhou, T. Seki, K. Takanashi, and T. Ono, Spin-orbit-torque memory operation of synthetic antiferromagnets, *Phys. Rev. Lett.* **121**, 167202 (2018).
- [8] R. A. Duine, K.-J. Lee, S. S. P. Parkin, and M. D. Stiles, Synthetic antiferromagnetic spintronics, *Nat. Phys.* **14**, 217 (2018).
- [9] S. Yang, T.-S. Ju, J. Seo, K.-W. Moon, C. Kim, H.-J. Kim, J. Shin, J. Yang, C. Hwang, and J. Hong, Ultralow-current magnetization switching in nearly compensated synthetic antiferromagnetic frames using sandwiched spin sources, *Acta Mater.* **208**, 116708 (2021).
- [10] S. Bandiera, R. C. Sousa, Y. Dahmane, C. Ducruet, C. Portemont, V. Baltz, S. Auffret, I. L. Prejbeanu, and B. Dieny, Comparison of synthetic antiferromagnets and hard ferromagnets as reference layer in magnetic tunnel junctions with perpendicular magnetic anisotropy, *IEEE Magn. Lett.* **1**, 3000204 (2010).
- [11] C.-Y. You, Effect of the synthetic antiferromagnetic polarizer layer rigidity on the spin transfer torque switching current density, *Appl. Phys. Lett.* **103**, 042402 (2013).

- [12] D. Houssameddine, J. F. Sierra, D. Guskova, B. Delaet, U. Ebels, L. D. Buda-Prejbeanu, M. C. Cyrille, B. Dieny, B. Ocker, J. Langer *et al.*, Spin torque driven excitations in a synthetic antiferromagnet, *Appl. Phys. Lett.* **96**, 072511 (2010).
- [13] Y. Shiota, T. Taniguchi, M. Ishibashi, T. Moriyama, and T. Ono, Tunable magnon-magnon coupling mediated by dynamic dipolar interaction in synthetic antiferromagnets, *Phys. Rev. Lett.* **125**, 017203 (2020).
- [14] A. Bergman, B. Skubic, J. Hellsvik, L. Nordström, A. Delin, and O. Eriksson, Ultrafast switching in a synthetic antiferromagnetic magnetic random-access memory device, *Phys. Rev. B* **83**, 224429 (2011).
- [15] D. Lyu, D. Zhang, D. B. Gopman, Y. Lv, O. J. Benally, and J.-P. Wang, Ferromagnetic resonance and magnetization switching characteristics of perpendicular magnetic tunnel junctions with synthetic antiferromagnetic free layers, *Appl. Phys. Lett.* **120**, 012404 (2022).
- [16] D. Lyu, J. E. Shoup, D. Huang, J. García-Barriocanal, Q. Jia, W. Echtenkamp, G. A. Rojas, G. Yu, B. R. Zink, X. Wang *et al.*, Sputtered $L1_0$ -FePd and its synthetic antiferromagnet on Si/SiO₂ wafers for scalable spintronics, *Adv. Funct. Mater.* **33**, 2214201 (2023).
- [17] B. Heinrich, G. Woltersdorf, R. Urban, and E. Simanek, Role of dynamic exchange coupling in magnetic relaxations of metallic multilayer films (invited), *J. Appl. Phys.* **93**, 7545 (2003).
- [18] A. J. Annunziata, P. L. Trouilloud, S. Bandiera, S. L. Brown, E. Gapihan, E. J. O'Sullivan, and D. C. Worledge, Materials investigation for thermally-assisted magnetic random access memory robust against 400 °C temperatures, *J. Appl. Phys.* **117**, 17B739 (2015).
- [19] H. Yang, Y. Li, and W. E. Bailey, Large spin pumping effect in antisymmetric precession of Ni₇₉Fe₂₁/Ru/Ni₇₉Fe₂₁, *Appl. Phys. Lett.* **108**, 242404 (2016).
- [20] K. Tanaka, T. Moriyama, M. Nagata, T. Seki, K. Takanashi, S. Takahashi, and T. Ono, Linewidth broadening of optical precession mode in synthetic antiferromagnet, *Appl. Phys. Express* **7**, 063010 (2014).
- [21] S. Sorokin, R. A. Gallardo, C. Fowley, K. Lenz, A. Titova, G. Y. P. Atcheson, G. Dennehy, K. Rode, J. Fassbender, J. Lindner *et al.*, Magnetization dynamics in synthetic antiferromagnets: Role of dynamical energy and mutual spin pumping, *Phys. Rev. B* **101**, 144410 (2020).
- [22] A. Kamimaki, S. Iihama, T. Taniguchi, and S. Mizukami, All-optical detection and evaluation of magnetic damping in synthetic antiferromagnet, *Appl. Phys. Lett.* **115**, 132402 (2019).
- [23] G. Wu, S. Chen, Y. Ren, Q. Y. Jin, and Z. Zhang, Laser-induced magnetization dynamics in interlayer-coupled [Ni/Co]₄/Ru/[Co/Ni]₃ perpendicular magnetic films for information storage, *ACS Appl. Nano Mater.* **2**, 5140 (2019).
- [24] G. Wu, S. Chen, S. Lou, Y. Liu, Q. Y. Jin, and Z. Zhang, Annealing effect on laser-induced magnetization dynamics in Co/Ni-based synthetic antiferromagnets with perpendicular magnetic anisotropy, *Applied Physics Letters* **115**, 142402 (2019).
- [25] G. Wu, W. Zhu, Z. Zhu, H. Xue, Y. Ren, Y. Liu, Q. Y. Jin, and Z. Zhang, Magnetic precession modes with enhanced frequency and intensity in hard/NM/soft perpendicular magnetic films, *Phys. Chem. Chem. Phys.* **21**, 16830 (2019).
- [26] S. Mangin, D. Ravelosona, J. A. Katine, M. J. Carey, B. D. Terris, and E. E. Fullerton, Current-induced magnetization reversal in nanopillars with perpendicular anisotropy, *Nat. Mater.* **5**, 210 (2006).

- [27] Y. Pogoryelov, M. Pereiro, S. Jana, A. Kumar, S. Akansel, M. Ranjbar, D. Thonig, D. Primetzhofer, P. Svedlindh, J. Åkerman *et al.*, Nonreciprocal spin pumping damping in asymmetric magnetic trilayers, *Phys. Rev. B* **101**, 054401 (2020).
- [28] T. Chiba, G. E. W. Bauer, and S. Takahashi, Magnetization damping in noncollinear spin valves with antiferromagnetic interlayer couplings, *Phys. Rev. B* **92**, 054407 (2015).
- [29] Y. Zhang, G. Wu, Z. Ji, X. Chen, Q. Y. Jin, and Z. Zhang, Significant and nonmonotonic dynamic magnetic damping in asymmetric Co-Fe/Ru/Co-Fe trilayers, *Phys. Rev. Appl.* **17**, 034033 (2022).
- [30] D. Huang, D. Lattery, and X. Wang, Materials engineering enabled by time-resolved magneto-optical Kerr effect for spintronic applications, *ACS Appl. Electron. Mater.* **3**, 119 (2021).
- [31] D. M. Lattery, J. Zhu, D. Huang, and X. Wang, Ultrafast thermal and magnetic characterization of materials enabled by the time-resolved magneto-optical Kerr effect, in *Nanoscale energy transport: Emerging phenomena, methods and applications*, edited by B. Liao (IOP Publishing, 2020), p. 9. <http://dx.doi.org/10.1088/978-0-7503-1738-2ch9>
- [32] D. M. Lattery, D. Zhang, J. Zhu, X. Hang, J. P. Wang, and X. Wang, Low Gilbert damping constant in perpendicularly magnetized W/CoFeB/MgO films with high thermal stability, *Sci. Rep.* **8**, 13395 (2018).
- [33] D. Huang, D. Lyu, X. Wang, M. B. Katz, D. Zhang, J.-P. Wang, D. B. Gopman, and X. Wang, Temperature-dependent perpendicular anisotropy and Gilbert damping of $L1_0$ -FePd films: Role of noble-metal buffer layers, *Phys. Rev. Mater.* **6**, 113402 (2022).
- [34] P. J. H. Bloemen, H. W. Van Kesteren, H. J. M. Swagten, and W. J. M. De Jonge, Oscillatory interlayer exchange coupling in Co/Ru multilayers and bilayers, *Phys. Rev. B* **50**, 13505 (1994).
- [35] See Supplemental Material at [URL to be inserted] for the analyses of the magnetization precession in each ferromagnetic layer; the estimation of each layer's contribution to total TR-MOKE signals; a summary of the parameters and uncertainties used in the data reduction; the impacts of α_1 , α_2 , and mutual spin pumping on phase; and the region diagrams for p-SAF with different degrees of asymmetries.
- [36] Z. Zhang, L. Zhou, P. E. Wigen, and K. Ounadjela, Angular dependence of ferromagnetic resonance in exchange-coupled Co/Ru/Co trilayer structures, *Phys. Rev. B* **50**, 6094 (1994).
- [37] B. Heinrich, Y. Tserkovnyak, G. Woltersdorf, A. Brataas, R. Urban, and G. E. W. Bauer, Dynamic exchange coupling in magnetic bilayers, *Phys. Rev. Lett.* **90**, 187601 (2003).
- [38] A. Brataas, Y. Tserkovnyak, G. E. W. Bauer, and B. I. Halperin, Spin battery operated by ferromagnetic resonance, *Phys. Rev. B* **66**, 060404(R) (2002).
- [39] Y. Tserkovnyak, A. Brataas, and G. E. W. Bauer, Spin pumping and magnetization dynamics in metallic multilayers, *Phys. Rev. B* **66**, 224403 (2002).
- [40] Y. Tserkovnyak, A. Brataas, and G. E. W. Bauer, Enhanced Gilbert damping in thin ferromagnetic films, *Phys. Rev. Lett.* **88**, 117601 (2002).
- [41] S. Iihama, S. Mizukami, H. Naganuma, M. Oogane, Y. Ando, and T. Miyazaki, Gilbert damping constants of Ta/CoFeB/MgO(Ta) thin films measured by optical detection of precessional magnetization dynamics, *Phys. Rev. B* **89**, 174416 (2014).
- [42] D. Zhang, D. Huang, R. J. Wu, D. Lattery, J. Liu, X. Wang, D. B. Gopman, K. A. Mkhoyan, J.-P. Wang, and X. Wang, Low Gilbert damping and high thermal stability of Ru-seeded $L1_0$ -phase FePd perpendicular magnetic thin films at elevated temperatures, *Appl. Phys. Lett.* **117**, 082405 (2020).

- [43] J. C. Slonczewski, Overview of interlayer exchange theory, *J. Magn. Magn. Mater.* **150**, 13 (1995).
- [44] J. C. Slonczewski, Fluctuation mechanism for biquadratic exchange coupling in magnetic multilayers, *Phys. Rev. Lett.* **67**, 3172 (1991).
- [45] W. Wang, P. Li, C. Cao, F. Liu, R. Tang, G. Chai, and C. Jiang, Temperature dependence of interlayer exchange coupling and Gilbert damping in synthetic antiferromagnetic trilayers investigated using broadband ferromagnetic resonance, *Appl. Phys. Lett.* **113**, 042401 (2018).
- [46] A. Kundu and S. Zhang, Temperature dependence of RKKY interaction, *J. Magn. Magn. Mater.* **393**, 331 (2015).
- [47] C. Y. You and S. C. Shin, Generalized analytic formulae for magneto-optical Kerr effects, *J. Appl. Phys.* **84**, 541 (1998).
- [48] A. J. Schellekens, K. C. Kuiper, R. R. J. C. de Wit, and B. Koopmans, Ultrafast spin-transfer torque driven by femtosecond pulsed-laser excitation, *Nat. Commun.* **5**, 4333 (2014).
- [49] B. Koopmans, G. Malinowski, F. Dalla Longa, D. Steiauf, M. Fähnle, T. Roth, M. Cinchetti, and M. Aeschlimann, Explaining the paradoxical diversity of ultrafast laser-induced demagnetization, *Nat. Mater.* **9**, 259 (2010).
- [50] G. Malinowski, F. Dalla Longa, J. H. H. Rietjens, P. V. Paluskar, R. Huijink, H. J. M. Swagten, and B. Koopmans, Control of speed and efficiency of ultrafast demagnetization by direct transfer of spin angular momentum, *Nat. Phys.* **4**, 855 (2008).
- [51] D. M. Lattery, J. Zhu, D. Zhang, J. P. Wang, P. A. Crowell, and X. Wang, Quantitative analysis and optimization of magnetization precession initiated by ultrafast optical pulses, *Appl. Phys. Lett.* **113**, 162405 (2018).
- [52] T. M. J. Cham, S. Karimeddiny, A. H. Dismukes, X. Roy, D. C. Ralph, and Y. K. Luo, Anisotropic gigahertz antiferromagnetic resonances of the easy-axis van der Waals antiferromagnet CrSBr, *Nano Letters* **22**, 6716 (2022).
- [53] Y. Shiota, T. Arakawa, R. Hisatomi, T. Moriyama, and T. Ono, Polarization-selective excitation of antiferromagnetic resonance in perpendicularly magnetized synthetic antiferromagnets, *Phys. Rev. Appl.* **18**, 014032 (2022).
- [54] D. H. Zanette, Energy exchange between coupled mechanical oscillators: linear regimes, *J. Phys. Commun.* **2**, 095015 (2018).
- [55] C. J. Durrant, L. R. Shelford, R. A. J. Valkass, R. J. Hicken, A. I. Figueroa, A. A. Baker, G. van der Laan, L. B. Duffy, P. Shafer, C. Klewe *et al.*, Dependence of spin pumping and spin transfer torque upon Ni₈₁Fe₁₉ thickness in Ta/Ag/Ni₈₁Fe₁₉/Ag/Co₂MnGe/Ag/Ta spin-valve structures, *Phys. Rev. B* **96**, 144421 (2017).
- [56] Y. Tserkovnyak, Ph.D., Harvard University, 2003.
- [57] B. Kardasz and B. Heinrich, Ferromagnetic resonance studies of accumulation and diffusion of spin momentum density in Fe/Ag/Fe/GaAs(001) and Ag/Fe/GaAs(001) structures, *Phys. Rev. B* **81**, 094409 (2010).
- [58] Y. Petrov, K. Migdal, N. Inogamov, V. Khokhlov, D. Ilnitsky, I. Milov, N. Medvedev, V. Lipp, and V. Zhakhovsky, Ruthenium under ultrafast laser excitation: Model and dataset for equation of state, conductivity, and electron-ion coupling, *Data in Brief* **28**, 104980 (2020).
- [59] A. Dabral, G. Pourtois, K. Sankaran, W. Magnus, H. Yu, A. de Jamblinne de Meux, A. K. A. Lu, S. Clima, K. Stokbro, M. Schaeckers *et al.*, Study of the intrinsic limitations of the

- contact resistance of metal/semiconductor interfaces through atomistic simulations, ECS Journal of Solid State Science and Technology **7**, N73 (2018).
- [60] B. Liu, D. Huang, M. Gao, H. Tu, K. Wang, X. Ruan, J. Du, J.-W. Cai, L. He, J. Wu *et al.*, The effect of growth sequence on magnetization damping in Ta/CoFeB/MgO structures, J. Magn. Mater. **450**, 65 (2018).
- [61] T. Kato, Y. Matsumoto, S. Kashima, S. Okamoto, N. Kikuchi, S. Iwata, O. Kitakami, and S. Tsunashima, Perpendicular anisotropy and Gilbert damping in sputtered Co/Pd multilayers, IEEE Trans. Magn. **48**, 3288 (2012).

Supplemental Material for

Magnetization Dynamics in Synthetic Antiferromagnets with Perpendicular Magnetic Anisotropy

Dingbin Huang^{1,*}, Delin Zhang², Yun Kim¹, Jian-Ping Wang², and Xiaojia Wang^{1,*}

¹Department of Mechanical Engineering, University of Minnesota, Minneapolis, MN 55455, USA

²Department of Electrical and Computer Engineering, University of Minnesota, Minneapolis, MN 55455, USA

Supplemental Note 1: Analyses of the magnetization precession in each Ferromagnetic (FM) layer

For the convenience of derivation, \mathbf{m}_i is represented in the spherical coordinates with the polar angle θ_i and the azimuthal angle φ_i , as shown in Fig. 1(b):

$$\mathbf{m}_i = (\sin \theta_i \cos \varphi_i, \sin \theta_i \sin \varphi_i, \cos \theta_i) \quad (\text{S1})$$

Accordingly, the expression of Eq. (2) in the spherical coordinates is:

$$\left\{ \begin{array}{l} \dot{\theta}_1 = \frac{-\gamma_1}{d_1 M_{s,1} \sin \theta_1} \frac{\partial F}{\partial \varphi_1} - \alpha_1 \sin \theta_1 \dot{\varphi}_1 + \alpha_{\text{sp},12} \sin \theta_2 \cos(\theta_2 - \theta_1) \dot{\varphi}_2 \\ \dot{\varphi}_1 = \frac{\gamma_1}{d_1 M_{s,1} \sin \theta_1} \frac{\partial F}{\partial \theta_1} + \frac{\alpha_1}{\sin \theta_1} \dot{\theta}_1 - \frac{\alpha_{\text{sp},12}}{\sin \theta_1} \dot{\theta}_2 \\ \dot{\theta}_2 = \frac{-\gamma_2}{d_2 M_{s,2} \sin \theta_2} \frac{\partial F}{\partial \varphi_2} - \alpha_2 \sin \theta_2 \dot{\varphi}_2 + \alpha_{\text{sp},21} \sin \theta_1 \cos(\theta_1 - \theta_2) \dot{\varphi}_1 \\ \dot{\varphi}_2 = \frac{\gamma_2}{d_2 M_{s,2} \sin \theta_2} \frac{\partial F}{\partial \theta_2} + \frac{\alpha_2}{\sin \theta_2} \dot{\theta}_2 - \frac{\alpha_{\text{sp},21}}{\sin \theta_2} \dot{\theta}_1 \end{array} \right. \quad (\text{S2})$$

* Authors to whom correspondence should be addressed: huan1746@umn.edu and wang4940@umn.edu

where, a dot over variables represents a derivative with respect to time. When \mathbf{M}_i precesses around its equilibrium direction:

$$\begin{cases} \theta_i = \theta_{0,i} + \Delta\theta_i \\ \varphi_i = \varphi_{0,i} + \Delta\varphi_i \end{cases} \quad (\text{S3})$$

with $\Delta\theta_i$ and $\Delta\varphi_i$ representing the deviation angles of \mathbf{M}_i from its equilibrium direction along the polar and azimuthal directions. Assuming the deviation is small, under the first-order approximation, the first-order partial derivative of F in Eq. (S2) can be expanded as:

$$\begin{cases} \frac{\partial F}{\partial \theta_i} \approx \frac{\partial^2 F}{\partial \theta_i^2} \Delta\theta_i + \frac{\partial^2 F}{\partial \varphi_i \partial \theta_i} \Delta\varphi_i + \frac{\partial^2 F}{\partial \theta_j \partial \theta_i} \Delta\theta_j + \frac{\partial^2 F}{\partial \varphi_j \partial \theta_i} \Delta\varphi_j \\ \frac{\partial F}{\partial \varphi_i} \approx \frac{\partial^2 F}{\partial \theta_i \partial \varphi_i} \Delta\theta_i + \frac{\partial^2 F}{\partial \varphi_i^2} \Delta\varphi_i + \frac{\partial^2 F}{\partial \theta_j \partial \varphi_i} \Delta\theta_j + \frac{\partial^2 F}{\partial \varphi_j \partial \varphi_i} \Delta\varphi_j \end{cases} \quad (\text{S4})$$

By substituting Eq. (S4), Equation (S2) is linearized as [1]:

$$\begin{bmatrix} \Delta\dot{\theta}_1 \\ \Delta\dot{\varphi}_1 \\ \Delta\dot{\theta}_2 \\ \Delta\dot{\varphi}_2 \end{bmatrix} = \mathbf{K} \begin{bmatrix} \Delta\theta_1 \\ \Delta\varphi_1 \\ \Delta\theta_2 \\ \Delta\varphi_2 \end{bmatrix} \quad (\text{S5})$$

where, \mathbf{K} is a 4×4 matrix, consisting of the properties of individual FM layers and the second-order derivatives of F in terms of θ_1 , φ_1 , θ_2 , and φ_2 . Equation (S5) has four eigen-solutions, in the form of $C \exp(i\omega t)$, corresponding to four precession frequencies: $\pm\omega^{\text{HF}}$ and $\pm\omega^{\text{LF}}$. A pair of eigen-solutions with the same absolute precession frequency are physically equivalent. Therefore, only two eigen-solutions need to be considered:

$$\begin{cases} \Delta\theta_i = C_{\theta,i}^{\text{HF}} \exp(i\omega^{\text{HF}} t) \\ \Delta\varphi_i = C_{\varphi,i}^{\text{HF}} \exp(i\omega^{\text{HF}} t) \end{cases} \text{ and } \begin{cases} \Delta\theta_i = C_{\theta,i}^{\text{LF}} \exp(i\omega^{\text{LF}} t) \\ \Delta\varphi_i = C_{\varphi,i}^{\text{LF}} \exp(i\omega^{\text{LF}} t) \end{cases} \quad (\text{S6})$$

After rearrangement, the full solutions in the spherical coordinates are expressed as below (also Eq. (3) in the main paper).

$$\begin{bmatrix} \theta_1(t) \\ \varphi_1(t) \\ \theta_2(t) \\ \varphi_2(t) \end{bmatrix} = \begin{bmatrix} \theta_{0,1} \\ \varphi_{0,1} \\ \theta_{0,2} \\ \varphi_{0,2} \end{bmatrix} + \begin{bmatrix} \Delta\theta_1(t) \\ \Delta\varphi_1(t) \\ \Delta\theta_2(t) \\ \Delta\varphi_2(t) \end{bmatrix} = \begin{bmatrix} \theta_{0,1} \\ \varphi_{0,1} \\ \theta_{0,2} \\ \varphi_{0,2} \end{bmatrix} + \begin{bmatrix} C_{\theta,1}^{\text{HF}} \\ C_{\varphi,1}^{\text{HF}} \\ C_{\theta,2}^{\text{HF}} \\ C_{\varphi,2}^{\text{HF}} \end{bmatrix} \exp(i\omega^{\text{HF}}t) + \begin{bmatrix} C_{\theta,1}^{\text{LF}} \\ C_{\varphi,1}^{\text{LF}} \\ C_{\theta,2}^{\text{LF}} \\ C_{\varphi,2}^{\text{LF}} \end{bmatrix} \exp(i\omega^{\text{LF}}t) \quad (\text{S7})$$

The prefactors of these eigen-solutions provide information about magnetization dynamics of both the HF and LF modes. Directly from solving Eq. (S2), one can obtain the relative ratios of these prefactors, which are $[C_{\varphi_1}^{\text{HF}}/C_{\theta_1}^{\text{HF}}, C_{\theta_2}^{\text{HF}}/C_{\theta_1}^{\text{HF}}, C_{\varphi_2}^{\text{HF}}/C_{\theta_1}^{\text{HF}}]$ and $[C_{\varphi_1}^{\text{LF}}/C_{\theta_1}^{\text{LF}}, C_{\theta_2}^{\text{LF}}/C_{\theta_1}^{\text{LF}}, C_{\varphi_2}^{\text{LF}}/C_{\theta_1}^{\text{LF}}]$. These ratios provide precession information of each mode, as presented in Fig. 3.

Obtaining the absolute values of $[C_{\theta,1}, C_{\varphi,1}, C_{\theta,2}, C_{\varphi,2}]^T$ for each mode requires the initial conditions of precession, which is necessary for fitting the actual precession amplitudes in TR-MOKE signals. In TR-MOKE measurements, magnetization precession is initiated by laser heating, which reduces the magnetic anisotropy of each FM layer and the interlayer exchange coupling strength between two FM layers [2]. Considering the laser heating process is ultrafast compared with magnetization precession while the following cooling due to heat dissipation is much slower than magnetization dynamics, we approximately model the temporal profiles of effective anisotropy fields and exchange coupling as step functions. Owing to the sudden change in magnetic properties induced by laser heating, magnetization in each layer will establish a new equilibrium direction $(\theta'_{0,i}, \varphi'_{0,i})$. In other words, \mathbf{M}_i deviates from its new equilibrium direction by $\Delta\theta_i = \theta_{0,i} - \theta'_{0,i}$, $\Delta\varphi_i = \varphi_{0,i} - \varphi'_{0,i}$. Substituting $t = 0$ to Eq. (S7), one can get the initial conditions for magnetization dynamics:

$$\begin{aligned} \Delta\theta_i(t=0) &= C_{\theta,i}^{\text{HF}} + C_{\theta,i}^{\text{LF}} = \theta_{0,i} - \theta'_{0,i} \\ \Delta\varphi_i(t=0) &= C_{\varphi,i}^{\text{HF}} + C_{\varphi,i}^{\text{LF}} = \varphi_{0,i} - \varphi'_{0,i} = 0 \end{aligned} \quad (\text{S8})$$

Once the initial conditions are set, the absolute values of all prefactors can be obtained.

Supplemental Note 2: Estimation of each layer's contribution to total TR-MOKE signals

The contribution from each FM layer is estimated by static MOKE measurement. According to Ref. [3], the result from this method matches well with that from the optical calculation. The sample is perpendicularly saturated before the static MOKE measurement. Then the out-of-plane M - H_{ext} loop (Fig. S1) is measured by static MOKE. As shown in the figure, two different antiferromagnetic (AF) configurations have different normalized MOKE signals, indicating the different contributions to the total signals by two layers. The weighting factor is calculated by:

$$-w + (1 - w) = 0.085 \quad (\text{S9})$$

which gives $w = 0.457$. Considering the relatively small layer thicknesses [FM₁: CoFeB(1), spacer: Ru(0.6)/Ta(0.3), and FM₂: Co(0.4)/Pd(0.7)/Co(0.4)], it is reasonable that FM₁ and FM₂ make comparable contributions to the total TR-MOKE signals (*i.e.*, $w \approx 0.5$).

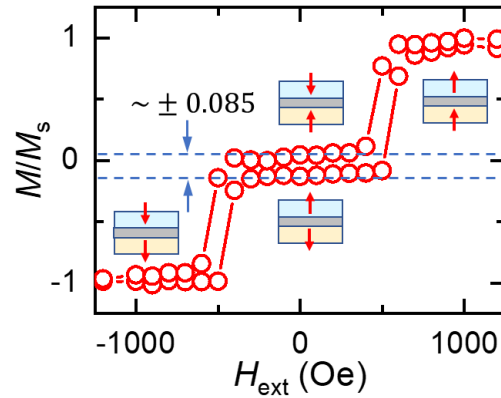


FIG. S1 Static MOKE hysteresis loop. Magnetic fields are applied along the out-of-plane direction.

Supplemental Note 3: Summary of the parameters and uncertainties for data reduction

Given that a number of variables are involved in the analysis, TABLE SI summarizes the major variables discussed in the manuscript, along with their values and determination methods.

TABLE SI. Summary of the values and determination methods of parameters used in the data reduction. The reported uncertainties are one-sigma uncertainties from the mathematical model fitting to the TR-MOKE measurement data.

Parameters	Values	Determination Methods
H_f	~ 500 Oe	VSM
$M_{s,1}$	1240 emu cm ⁻³	VSM
$M_{s,2}$	827 emu cm ⁻³	VSM
d_1	1 nm	Sample structure
d_2	1.5 nm	Sample structure
$H_{k,eff,1}$	1.23 ± 0.28 kOe	Fitted from f vs. H_{ext} [Fig. 2(b)]
$H_{k,eff,2}$	6.18 ± 0.13 kOe	Fitted from f vs. H_{ext} [Fig. 2(b)]
γ_1	17.79 ± 0.04 rad ns ⁻¹ kOe ⁻¹	Fitted from f vs. H_{ext} [Fig. 2(b)]
γ_2	17.85 ± 0.04 rad ns ⁻¹ kOe ⁻¹	Fitted from f vs. H_{ext} [Fig. 2(b)]
J_1	-0.050 ± 0.020 erg cm ⁻²	Fitted from f vs. H_{ext} [Fig. 2(b)]
J_2	0	Fitted from f vs. H_{ext} [Fig. 2(b)]
w	0.457	Static MOKE
$H'_{k,eff,1}/H_{k,eff,1}$	0.90 ± 0.01	Fitted from Amp vs. H_{ext} [Fig. 4(a)]
$H'_{k,eff,2}/H_{k,eff,2}$	0.95 ± 0.01	Fitted from Amp vs. H_{ext} [Fig. 4(a)]
J'_1/J_1	0.83 ± 0.01	Fitted from Amp vs. H_{ext} [Fig. 4(a)]
α_1	0.020 ± 0.002	Fitted from α_{eff} vs. H_{ext} [Fig. 5(a)] and β vs. H_{ext} [Fig. 4(c)]
α_2	0.060 ± 0.008	Fitted from α_{eff} vs. H_{ext} [Fig. 5(a)] and β vs. H_{ext} [Fig. 4(c)]
$\Delta H_{k,eff,1}$	0.26 ± 0.02 kOe	Fitted from α_{eff} vs. H_{ext} [Fig. 5(a)]
$\Delta H_{k,eff,2}$	1.42 ± 0.18 kOe	Fitted from α_{eff} vs. H_{ext} [Fig. 5(a)]
$\alpha_{sp,12}$	0.010 ± 0.004	Fitted from α_{eff} vs. H_{ext} [Fig. 5(a)] and β vs. H_{ext} [Fig. 4(c)]
$\alpha_{sp,21}$	$0.007^{+0.009}_{-0.007}$	Fitted from α_{eff} vs. H_{ext} [Fig. 5(a)] and β vs. H_{ext} [Fig. 4(c)]

Supplemental Note 4: Impacts of α_1 , α_2 , and mutual spin pumping on the phase

Without damping, the phase difference in the precession polar angles of two FM layers [$\text{Arg}(C_{\theta_2}/C_{\theta_1})$] is always 0° or 180° , as shown in Fig. 3 of the main article. However, this does not necessarily hold if either the damping or mutual spin pumping is considered. The changes in the phase difference due to damping are depicted in Fig. S2. When $\alpha_1 = \alpha_2$, the phase difference between two layers stays at 0° or 180° [Fig. S2(a)], identical to the lossless case ($\alpha_1 = \alpha_2 = 0$) in Fig. 3. As a result, the initial phase of TR-MOKE signals (β) also stays at 0° or 180° [Fig. S2(b)]. However, when $\alpha_1 \neq \alpha_2$, $\text{Arg}(C_{\theta_2}/C_{\theta_1})$ deviates from 0° or 180° especially at high fields ($H_{\text{ext}} > 5$ kOe) [Fig. S2(c,e)]. The layer with a higher damping [FM₁ in (c) or FM₂ in (e)] tends to have a more advanced phase at high fields (regions 2 and 3). For example, in Fig. S2(e), $0^\circ < \text{Arg}(C_{\theta_2}/C_{\theta_1}) < 180^\circ$ for both HF and LF modes in regions 2 and 3. The deviation from the perfect in-phase (0°) or out-of-phase (180°) condition allows the IEC to transfer energy from the low-damping layer to the high-damping layer, such that the precession in both layers can damp at the same rate [4]. As a result, the initial phase of the TR-MOKE signals also changes, which opens a negative or positive gap at high fields (> 10 kOe) for both modes, as shown in Fig. S2(d,f). This enables us to determine the difference between α_1 and α_2 by analyzing the initial phase of TR-MOKE signals.

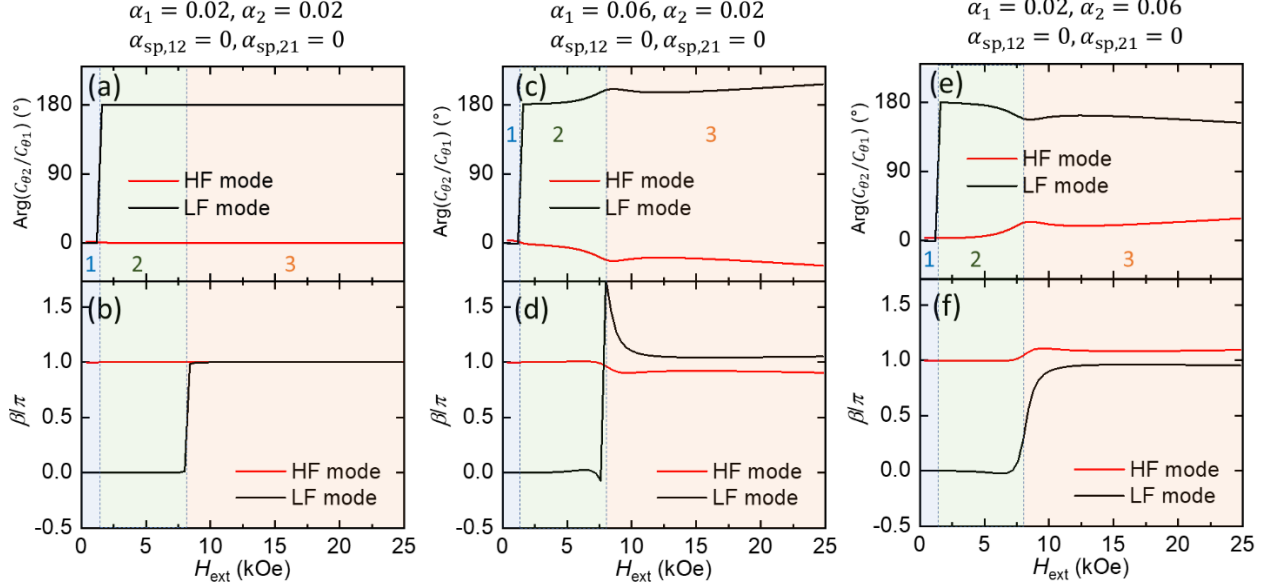


FIG. S2 Impact of α_1 and α_2 on the phase without mutual spin pumping. (a,c,e) The phase difference between the polar angles in two layers for HF and LF modes. (b,d,f) The calculated initial phase of TR-MOKE signals for each mode with $\alpha_1 = \alpha_2 = 0.02$ (a,b), $\alpha_1 = 0.06$ and $\alpha_2 = 0.02$ (c,d), and $\alpha_1 = 0.02$ and $\alpha_2 = 0.06$ (e,f). The mutual spin pumping is set as $\alpha_{sp,12} = \alpha_{sp,21} = 0$ for all three cases. The rest of the parameters used in this calculation can be found in TABLE SI.

The impact of mutual spin pumping on the precession phase is illustrated in Fig. S3, where three different cases of either the one-way ($\alpha_{sp,12}$ or $\alpha_{sp,21}$) or two-way (both $\alpha_{sp,12}$ and $\alpha_{sp,21}$) spin pumping are considered. A reference case without the consideration of mutual spin pumping ($\alpha_1 = 0.02$, $\alpha_2 = 0.06$, and $\alpha_{sp,12} = \alpha_{sp,21} = 0$) is also plotted (dashed curves) for the ease of comparison. In general, it can be seen that mutual spin pumping could also change the phase difference in the precession polar angles of two layers, and thus the initial phase of TR-MOKE signals noticeably. This can be explained by the damping modification resulting from spin pumping. In regions 2 and 3, Eq. (2) can be approximately rearranged as:

$$\begin{aligned}
\frac{d\mathbf{m}_i}{dt} &\approx -\gamma_i \mathbf{m}_i \times \mathbf{H}_{\text{eff},i} + \alpha_i \mathbf{m}_i \times \frac{d\mathbf{m}_i}{dt} - \frac{C_j}{C_i} \alpha_{\text{sp},ij} \cos(\theta_{0,1} - \theta_{0,2}) \mathbf{m}_i \times \frac{d\mathbf{m}_i}{dt} \\
&\approx -\gamma_i \mathbf{m}_i \times \mathbf{H}_{\text{eff},i} + \left[\alpha_i - \frac{C_j}{C_i} \alpha_{\text{sp},ij} \cos(\theta_{0,1} - \theta_{0,2}) \right] \mathbf{m}_i \times \frac{d\mathbf{m}_i}{dt} \\
&= -\gamma_i \mathbf{m}_i \times \mathbf{H}_{\text{eff},i} + \bar{\alpha}_i \mathbf{m}_i \times \frac{d\mathbf{m}_i}{dt}
\end{aligned} \tag{S10}$$

where C_j/C_i represents the ratio of the cone angles in the j -th FM layer to the i -th FM layer. C_j/C_i is positive for the in-phase mode and negative for the out-of-phase mode. $\theta_{0,1}$ and $\theta_{0,2}$ are the equilibrium polar angles of \mathbf{M}_1 and \mathbf{M}_2 , as defined in Fig. 2(c). Therefore, the mutual spin-pumping term either enhances or reduces the damping depending on the mode. $\bar{\alpha}_i = \alpha_i - \frac{C_j}{C_i} \alpha_{\text{sp},ij} \cos(\theta_{0,1} - \theta_{0,2})$ represents the effective Gilbert damping in the i -th FM layer after considering the mutual spin-pumping effect. This modification to damping is more significant when the i -th layer is subservient with a smaller cone angle (*e.g.*, FM₂ for the HF mode in region 3), while the j -th layer is dominant with a much larger precession cone angle (*e.g.*, FM₁ for the LF mode in region 3), leading to a large ratio of $|C_j/C_i|$.

In Fig. S3(a), only the spin current injected from FM₁ to FM₂ is considered. According to the above analysis, $\alpha_{\text{sp},21}$ can only bring noticeable modifications to the damping of FM₂ when FM₁ is the dominant layer. Based on Fig. 3 in the main article, the LF mode in region 2 and HF mode in region 3 satisfy this condition (FM₁ dominant and FM₂ subservient). As shown in Fig. S3(a), the phase difference noticeably deviates from the reference case without mutual spin pumping (dashed curves) in region 2 for the LF mode (black curves) and in region 3 for the HF mode (red curves). For the LF mode in region 2, the precession motions in two layers are nearly out-of-phase (negative C_1/C_2); therefore, the spin pumping from FM₁ enhances the damping in FM₂. Since α_1 (0.02) is less than α_2 (0.06), the spin pumping from FM₁ to FM₂ further increases $|\bar{\alpha}_1 - \bar{\alpha}_2|$ between the two layers. Consequently, the phase difference shifts further away from 180°. While

for the HF mode in region 3, $\alpha_{\text{sp},21}$ reduces the damping of FM₂ because C_1/C_2 is positive resulting from the near in-phase feature of this mode. Hence, $|\bar{\alpha}_1 - \bar{\alpha}_2|$ becomes smaller and the phase difference gets closer to 0° . In Fig. S3(c), only $\alpha_{\text{sp},12}$ is considered, which requires FM₂ as the dominant layer (the HF mode in region 2 and LF mode in region 3) for noticeable changes in $|\bar{\alpha}_1 - \bar{\alpha}_2|$. For the HF mode in region 2, spin pumping from FM₂ reduces $\bar{\alpha}_1$ given that the precession motions in two layers are nearly in phase (positive C_2/C_1). Therefore, $|\bar{\alpha}_1 - \bar{\alpha}_2|$ increases and the phase difference in Fig. S3(c) shifts further away from 0° in region 2. However, for the LF mode in regions 3, the nearly out-of-phase precession in two FM layers (negative C_1/C_2) increases $\bar{\alpha}_1$ and reduces $|\bar{\alpha}_1 - \bar{\alpha}_2|$. As a result, the phase difference in Fig. S3(c) shifts toward 180° . When both $\alpha_{\text{sp},12}$ and $\alpha_{\text{sp},21}$ are considered [Fig. S3(e)], a combined effect is expected for the phase difference with noticeable changes for both the HF and LF modes in regions 2 and 3.

The impacts of mutual spin pumping on the phase difference between the HF and LF modes are reflected by the initial phase of TR-MOKE signals [β in Fig. S3(b,d,f)]. Compared with the reference case without mutual spin pumping (dashed curves), the introduction of mutual spin pumping tends to change the gap in β between the two modes. As shown in Fig. S3(e,f), the values of two mutual-spin-pumping induced damping terms are chosen as $\alpha_{\text{sp},12} = 0.013$ and $\alpha_{\text{sp},21} = 0.004$, such that the β gap of the initial phase of TR-MOKE signals is closed at high fields (region 3). Therefore, the initial phase of TR-MOKE signals provides certain measurement sensitivities to $\alpha_{\text{sp},12}$ and $\alpha_{\text{sp},21}$, which enables us to extract the values of $\alpha_{\text{sp},ij}$ from measurement fitting. Here, we acknowledge that the measurement sensitivity to $\alpha_{\text{sp},ij}$ from TR-MOKE is limited, which subsequently leads to relatively large error bars for $\alpha_{\text{sp},ij}$ (see Table SI).

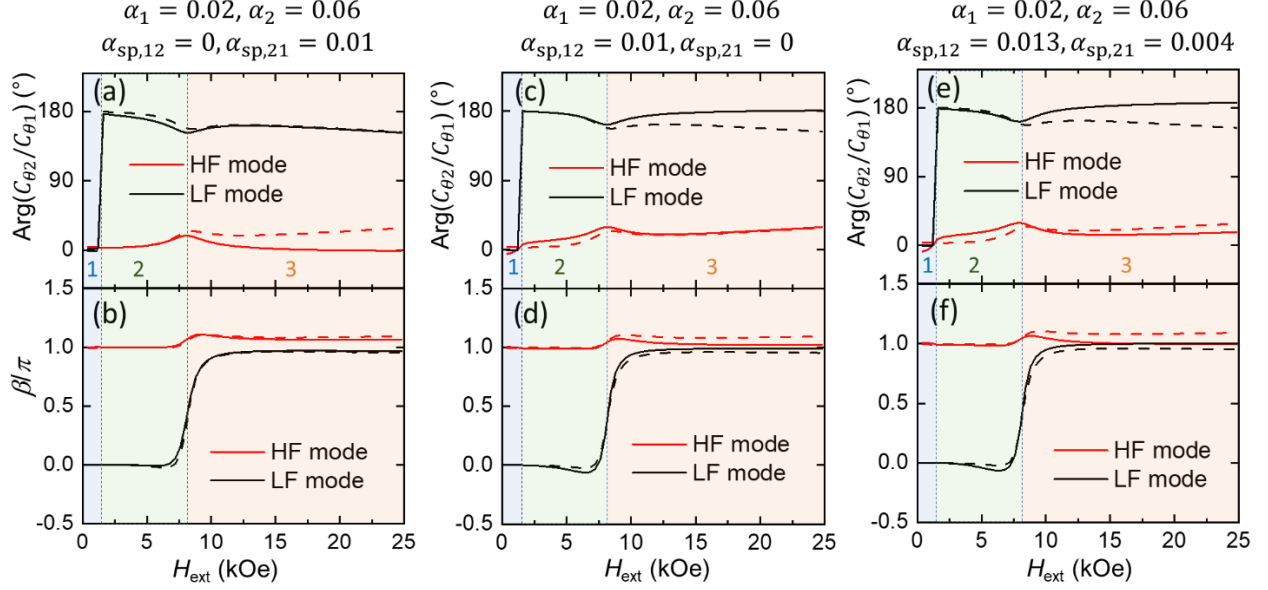


FIG. S3 Impact of mutual spin pumping on the phase with fixed damping values of $\alpha_1 = 0.02$ and $\alpha_2 = 0.06$. (a,c,e) The phase difference between the polar angles in two layers for HF and LF modes. (b,d,f) The calculated initial phase of TR-MOKE signals (β) for each mode with $\alpha_{sp,12} = 0$ and $\alpha_{sp,21} = 0.01$ (a,b), $\alpha_{sp,12} = 0.01$ and $\alpha_{sp,21} = 0$ (c,d), and $\alpha_{sp,12} = 0.013$ and $\alpha_{sp,21} = 0.004$ (e,f). For the third case (e,f), the values of mutual spin pumping are chosen to close the β gap in panel (f) for $H_{ext} > 15$ kOe. The rest of the parameters used in this calculation can be found in TABLE SI. Dashed lines represent the reference case without mutual spin pumping ($\alpha_1 = 0.02$, $\alpha_2 = 0.06$, and $\alpha_{sp,12} = \alpha_{sp,21} = 0$).

Supplemental Note 5: Region diagrams for p-SAFs with different degrees of asymmetries

Figure S4 shows the region diagrams for p-SAFs with different degrees of asymmetries, represented by the difference of $H_{k,eff}$ in two FM layers. $H_{k,eff,1} = H_{k,eff,2}$ corresponds to the symmetric case (lowest asymmetry), as shown by Fig. S4(c). While the SAF in Fig. S4(a) has the highest asymmetry: $H_{k,eff,1} = 2$ kOe, $H_{k,eff,2} = 6$ kOe. Figure S4 clearly shows that $|\theta_{0,1} - \theta_{0,2}| > 90^\circ$ is a necessary but not sufficient condition for region 1 (CW precession). Because regions 2 or 3 also appear to the left of the red curve (where $|\theta_{0,1} - \theta_{0,2}| > 90^\circ$), especially when θ_H is close to 90° and $H_{k,eff,1}$ is close to $H_{k,eff,2}$.

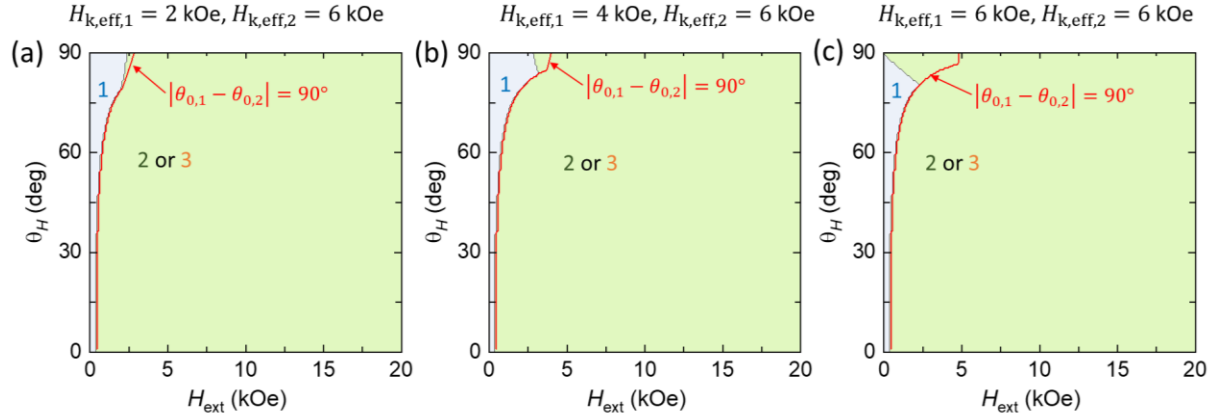


FIG. S4 Region diagrams of p-SAFs with different degrees of asymmetries: $H_{k,\text{eff},1} = 2 \text{ kOe}$, $H_{k,\text{eff},2} = 6 \text{ kOe}$ (a), $H_{k,\text{eff},1} = 4 \text{ kOe}$, $H_{k,\text{eff},2} = 6 \text{ kOe}$ (b), $H_{k,\text{eff},1} = 6 \text{ kOe}$, $H_{k,\text{eff},2} = 6 \text{ kOe}$ (c). The blue background represents region 1. The green background covers regions 2 and 3. The red curve shows the conditions where $|\theta_{0,1} - \theta_{0,2}| = 90^\circ$. $|\theta_{0,1} - \theta_{0,2}| > 90^\circ$ to the left of the red curve. α_1 , α_2 , $\alpha_{\text{sp},12}$, and $\alpha_{\text{sp},21}$ are set as zero. $\gamma_1 = \gamma_2 = 17.8 \text{ rad ns}^{-1} \text{ kOe}^{-1}$. Values of the rest parameters are the same as those in Table SI.

References

- [1] Z. Zhang, L. Zhou, P. E. Wigen, and K. Ounadjela, Angular dependence of ferromagnetic resonance in exchange-coupled Co/Ru/Co trilayer structures, *Phys. Rev. B* **50**, 6094 (1994).
- [2] W. Wang, P. Li, C. Cao, F. Liu, R. Tang, G. Chai, and C. Jiang, Temperature dependence of interlayer exchange coupling and Gilbert damping in synthetic antiferromagnetic trilayers investigated using broadband ferromagnetic resonance, *Appl. Phys. Lett.* **113**, 042401 (2018).
- [3] G. Malinowski, F. Dalla Longa, J. H. H. Rietjens, P. V. Paluskar, R. Huijink, H. J. M. Swagten, and B. Koopmans, Control of speed and efficiency of ultrafast demagnetization by direct transfer of spin angular momentum, *Nat. Phys.* **4**, 855 (2008).
- [4] D. H. Zanette, Energy exchange between coupled mechanical oscillators: linear regimes, *J. Phys. Commun.* **2**, 095015 (2018).